Journal of the Meteorological Society of Japan

EARLY ONLINE RELEASE

The DOI for this manuscript is
DOI:10.2151/jmsj.2025-007
J-STAGE Advance published date: December 10, 2024
The final manuscript after publication will replace the preliminary version at the above DOI once it is available.

Nonlinear Perturbation Growth at Mesoscale Related to Upscaling Processes from a Mesoscale Convective System

Kosuke ONO[1]

Meteorological Research Institute, Japan Meteorological Agency, Tsukuba, Japan

Graduate School of Science, Hokkaido University, Sapporo, Japan

and

Masaru INATSU

Faculty of Science and Center for Natural Hazards Research, Hokkaido University, Sapporo, Japan

(Manuscript submitted October 13, 2023, in a revised form 28 August 2024)

----

1) Corresponding author: Kosuke Ono, Meteorological Research Institute, Japan Meteorological Agency, 1-1, Nagamine, Tsukuba, Ibaraki 305-0052 JAPAN

Email: onok@mri-jma.go.jp

Tel: +81-29-853-8552

Abstract

In this study, the nonlinearity in a weather forecast was examined in an environment containing a mesoscale convective system. The nonlinearity was quantified by the relative nonlinearity as the extent to which the initial opposite-sign perturbed state vector does not keep the same magnitude and opposite direction in a forecast time. A pair of 18-h forecast experiments with initial perturbations of different signs was conducted for a heavy rainfall event in western Japan on 13 August 2021.

Despite the initially different signs, the perturbations had random structures at convective scales over 2 h, taking the relative nonlinearity value 1.72 as previous studies have shown. However, the perturbations had the same sign on the meso-α scale at 11 h, taking the relative nonlinearity value greater than 1.72. This result suggested that this nonlinear signal was found not only on the convective scale but also on the meso-α scale. The nonlinear signal upscaled from convective to mesoscale, indicating a transition to a nonlinear regime at the mesoscale. Additional experiments showed that this meso-α scale nonlinear signal originated from the front with high convective activities in the initial field through the emission of gravity waves via the moist physics.

Keywords perturbation growth; nonlinearity; mesoscale convective system; upscaling

1. Introduction

Ensemble forecasts have been introduced in short-term weather forecasting to offer practical predictability information (e.g. Kühnlein et al. 2014; Raynaud and Bouttier, 2017; Ono et al. 2021). Assuming that the initial perturbations grow linearly in time, a pair of opposite-sign initial perturbations is usually input into a synoptic forecast system to generate as many forecast varieties as possible, similar to global ensemble predictions (e.g., Wang et al. 2014; Ono et al. 2021). However, the growth of initial perturbations in a forecasting model could violate the assumption of linear growth as the atmosphere is a nonlinear dynamical system. Hohenegger and Schär (2007a) demonstrated that runs with different initial perturbations imposed in their cloud-resolving model provided similar spatial patterns of perturbations after 11 h. This change in perturbation growth direction indicates nonlinearity, as perturbations do not propagate linearly to retain the same direction. Thus, the similar spatial patterns seen in forecasts from different initial perturbations can be interpreted as a “nonlinear signal”. This paper investigates atmospheric nonlinearity as a dynamical system by examining this nonlinear signal, with the aim of improving ensemble prediction system design.

To design mesoscale model ensemble forecasts better, it is necessary to understand the characteristics of the initial perturbation growth in ensemble forecasts, particularly when the growth is nonlinear. Research on the perturbation magnitude growth of initial perturbations has hinted at changes in perturbation growth direction observed in mesoscale model forecasts (e.g., Sun and Zhang 2016; Weyn and Durran 2017; Wu and Takemi 2023; Minamide et al. 2020). Zhang et al. (2007) attributed the fast growth of small-scale perturbations to convective instability over the first few forecast hours, whereas they attributed the slow growth of synoptic perturbations to baroclinic instability on a daily timescale. In mesoscale convective systems (MCSs), the meso-β scale (20–200 km) initial perturbation downscales rapidly, and then upscales (Durran and Weyn 2016). The upscale energy cascade through gravity wave excitation and resultant geostrophic adjustment may enlarge the convective-scale perturbation at the meso-γ scale (2–20 km) to the meso-β scale or even the meso-α scale (200–2000 km; Selz and Craig 2015), as suggested theoretically (Bierdel et al. 2017) or by idealized experiments (Bierdel et al. 2018). Rodwell et al. (2013) showed that the convective activity in the United States degraded the synoptic wave forecast in Europe through upscaling.

The above studies highlight the importance of the error growth in magnitude upscaling from the convective scale. This suggests that a nonlinear signal—namely, changes in perturbation growth direction-- in mesoscale model forecasts may also be related to a type of upscaling. Previous studies have explored the nonlinearity of the atmosphere by assessing the error growth direction at a convective scale (Hohenegger and Schär 2007b) and larger scales (Gilmour et al. 2001). However, there is a lack of literature that elaborates on the changes in error growth direction at the mesoscale. The nonlinear signal's upscaling process may eventually distort the linear assumption at mesoscales, same as synoptic scales demonstrated by Gilmour (2001). It remains an unanswered question about how the nonlinear signal behaves between convective scales and mesoscales.

The purpose of this study is to assess the nonlinearity of an MCS with multiscale features by analyzing the growth direction of perturbation pairs with initially opposite sign. We investigated the nonlinear signal at both convective and mesoscales to see if there was an upscaling feature by conducting a plausible set of initial perturbation growth experiments with an operational mesoscale forecast system of the Japan Meteorological Agency (JMA). Spatial filtering was applied to the model perturbation at all forecast times to emphasize the upscaling of the perturbation structures with time.

According to Lin (2006), an MCS is classified four types of mesoscale phenomena, such as squall lines, mesoscale convective complexes in the midlatitudes, tropical cyclone, and cloud clusters in the tropics. This study focused on the squall line type of an MCS, called a line-shaped rain band which is frequently observed in western Japan in the summertime Asian monsoon environment (Hirockawa et al. 2020). The line-shaped rainband composes organized cumulonimbuses and maintains its strong convective activity by the back building type formation (Bluestain and Jain 1985; Kato 2020). We conducted a pair of 18-h forecast experiments with initial perturbations of different signs for a heavy rainfall event related to a line-shaped rainband along with the shear zone on the persistent Baiu front in western Japan on 13 August 2021 (Fig.1). We chose this event because the line-shaped rainband is an MCS that contains a multiscale structure, from the upper-level cold low to the lower-level water vapor flow (e.g., Kawano and Kawamura 2020) and is characterized by a persistent strong convective activity. These facts are favorable to analyze upscaling processes for the initial perturbations.

The remainder of this paper is organized as follows. Section 2 describes the forecast model and the initial perturbation method used in this study. Section 3 explains the metric for evaluating nonlinear signals and spatial filtering. Section 4 presents the results on the nonlinear signals in the perturbations in our forecast experiments. Section 5 provides our conclusions and discusses the interpretation of the results.

2. Experimental settings

2.1 Model

As the regional forecast model, we used A System based on a Unified Concept for Atmosphere (ASUCA; Ishida et al. 2022), which is part of the JMA's operational forecasting system, as of May 2024. We set the model configuration as in the operational local forecast model (LFM; JMA 2022) with a horizontal grid spacing of 2 km, but the forecasting period was extended to 18 h. The forecast domain was the whole region shown in Fig. 2a, which was composed of 1585 × 1305 horizontal grid points. The hybrid terrain-following vertical coordinate was adopted with 76 layers. The depth of vertical layers increased with height from 20 m at the lowest layer to about 650 m at the highest [see Fig. B1 of Ishida et al. (2022) for more details]. The forecast variables of ASUCA are density, momentum, potential temperature, water vapor, and water substances. The planetary-boundary-layer mixing processes are based on Mellor–Yamada–Nakanishi–Niino Level-3 scheme (Nakanishi and Niino 2009); and the surface flux is based on Monin–Obukhov similarity theory (Beljaars and Holtslag 1991). Cloud physics was based on the single-moment, three-ice bulk method (JMA 2022). Cumulus convection was then represented explicitly, except for the convection initiation (Hara 2015), which was parameterized based on the Kain-Fritsch scheme (Kain and Fritsch 1990)[1].

Initial conditions for the LFM were generated by the three-dimensional variational data assimilation, which assimilates radial velocity and reflectivity from doppler radars to help the spin-up in convective regions (Ikuta et al. 2021). The lateral boundary conditions for the LFM were provided by the JMA's operational mesoscale model (JMA 2022) with a horizontal grid spacing of 5 km.

2.2 Initial perturbation

The initial perturbations were made by the breeding of growing mode method (Toth and Kalnay 1993), which sought a set of the perturbations with the greatest growth in the

[1] Hara (2015) showed that the LFM could not forecast lower-layer convergence smaller than the grid scale that triggers convection without cumulus convection parameterization, resulting in a delay in the initiation of convection. To address this issue, in the LFM, the vertical transport of heat, water vapor, and cloud water were parameterized in slightly unstable stratifications by activating the cumulus parameterization based on the Kain–Fritsch scheme (Kain and Fritsch 1990) at each timestep only for convective initiation. The effects of the parameterization on the forecast variables were weaker than those of the original Kain–Fritsch scheme (Hara 2015).

model run (Fig. 3a). The lateral boundary perturbations for horizontal wind, temperature, and water vapor mixing ratio were obtained from the JMA's global ensemble prediction system in advance (JMA 2022). We did not calculate the lower boundary perturbations and physics perturbations in the following breeding cycle.

The 54 h until the target event started, that is, the period from 0000 UTC 11 August 2021 to 0600 UTC 13 August, were allocated for the breeding process with its 6 h cycle (Fig. 3a). First, we prepared the control run with a control lateral boundary condition in this 54-h breeding period. Next, the model ran in a breeding run for 6 h, from the initial condition with a perturbed lateral boundary condition. The initial perturbations were not used at the start of the breeding cycle, but were created at 0600 UTC 11 August after the first breeding cycle (Fig. 3a). The breeding run was restarted from the rescaling state plus the control run's result at 6 h of breeding, and the model ran for the next 6 h. The difference between breeding and control runs at 6 h of breeding, for example, 1200 UTC 11 August in this case, was rescaled (broken lines in Fig. 3a) to a magnitude comparable to those in the JMA's current mesoscale ensemble prediction system [horizontal wind ~ 1.8 m s^{-1}, temperature ~ 0.7 K, and water vapor mixing ratio ~ 1.0 g kg^{-1} after Ono et al. (2021)]. By repeating this procedure for a further 54 h of breeding, we obtained the fastest-growing perturbation called "the first bred vector".

The rescaling and normalization in the breeding process require the norm and the associated inner product. We used the total energy norm for the perturbed state vector of $\boldsymbol{\delta x} = (\delta u\ \delta v\ \delta\theta\ \delta q\ \delta p_s)^{\mathbf{T}}$ over model domain S (Ehrendorfer et al. 1999) defined by

$$\|\boldsymbol{\delta x}\|_S^2 = \int_{z_1}^{z_2}\int_S \frac{\rho}{2}\left(\delta u^2 + \delta v^2 + \frac{C_p}{\Theta_r}\delta\theta^2 + \frac{RT_r}{P_r^2}\delta \mathrm{p}_s^2 + \frac{L^2}{C_pT_r}\delta q^2\right) dS\, dz\,, \tag{1}$$

where ρ is density; δu and δv are zonal and meridional wind perturbations, respectively; $\delta\theta$, δp_s, and δq are perturbations of potential temperature, surface pressure, and water vapor mixing ratio, respectively; $C_p = 1005.7\ \mathrm{J\ kg^{-1}\ K^{-1}}$ is the specific heat at constant pressure; $\Theta_r = 300\ \mathrm{K}$, $T_r = 300\ \mathrm{K}$, and $P_r = 10^5\ \mathrm{Pa}$ are the reference values of potential temperature, temperature, and pressure, respectively; $R = 287.04\ \mathrm{J\ kg^{-1}\ K^{-1}}$ is the gas constant for dry air; and $L = 2.51 \times 10^6\ \mathrm{J\ kg^{-1}}$ is the latent heat of vaporization. We set z_1 as the lowermost model level and z_2 as the 53rd model level (~9500 m). The associated inner product was also defined as

$$(\boldsymbol{\delta x_1},\boldsymbol{\delta x_2})_S = \int_{z_1}^{z_2}\int_S \frac{\rho}{2}\left(\delta u_1\delta u_2 + \delta v_1\delta v_2 + \frac{C_p}{\Theta_r}\delta\theta_1\delta\theta_2 + \frac{RT_r}{P_r^2}\delta \mathrm{p}_{s,1}\,\delta \mathrm{p}_{s,2} + \frac{L^2}{C_pT_r}\delta q_1\delta q_2\right) dS\, dz, \tag{2}$$

for $\boldsymbol{\delta x_1} = (\delta u_1\ \delta v_1\ \delta\theta_1\ \delta q_1\ \delta p_{s,1})^{\mathbf{T}}$ and $\boldsymbol{\delta x_2} = (\delta u_2\ \delta v_2\ \delta\theta_2\ \delta q_2\ \delta p_{s,2})^{\mathbf{T}}$.

2.3 Forecast runs

We performed the control forecast run (run C) and 10 pairs of positive and negative initially perturbed forecast runs (Table 1). All forecasts were initialized at 0600 UTC on 13 August 2021 and run for 18 h with no perturbations applied to the lower and lateral boundaries or physics (Fig. 3b). No perturbations from lateral boundaries affected the perturbation growth in domain K until the end of the forecast (not shown); thus, we only handled the initial perturbation growth in the whole forecast domain. This was because the atmospheric flow around Japan was slower in summer than in winter owing to the prevailing stronger jet streams. Run C was performed with no initial perturbations over the model domain.

A pair of perturbed forecast runs were performed with the first bred vector added to the control's initial conditions. Because the sign of the perturbation was arbitrary, two opposite directions could be chosen in the first bred vector. We nominated one direction as run P and the other as run N. The meaning of P and N is positive and negative, regardless of the sign in the real field of any variables, as in Fig. 2. For example, run P gave an initial perturbation field of meridional wind on the 21st model level (~850 hPa; Fig. 2b). In run N, the initial perturbation with the opposite sign (Fig. 2c) was added to the control's initial field. The perturbations were on the convective scale and mesoscale and had large magnitudes along the stationary front, where the strong rainfall was observed (Fig. 1c). In contrast, the perturbations had smaller magnitudes and a larger scale near the lateral boundaries, reflecting the perturbation from the global ensemble prediction system. The perturbation magnitudes were much smaller on the southeastern side of the domain where the subtropical high prevailed (Figs. 2b,c).

Additional pairs of positive and negative perturbation runs were performed to detect the origin of the nonlinearity in the initial field. In these runs, the initial perturbations based on the first bred vector were confined to a 40-km radius centered at 32°N, 127°E (runs pF and nF) and 33°N, 129°E (runs pF' and nF'), where the heavy rainfall was observed in the targeted event on the stationary front. Additionally, the initial perturbations were confined by both above two circles (runs pF'' and nF''). The initial perturbations were also confined to a 40-km radius centered at 28°N, 131°E (runs pS and nS) and 32°N, 131°E (runs pS' and nS') on the southern side of the heavy rainfall area on the stationary front.

We also investigated the sensitivity of the perturbed variables at the initial time by modifying runs pF'' and nF'' through the limiting wind, potential temperature, and water vapor perturbations, and these runs were called pW, nW, pT, nT, pQ, and nQ, respectively. Runs pD and nD investigated the importance of moist physics to the nonlinear signals. These runs were same as runs pF'' and nF'' without the convective parameterization and the cloud microphysics in the model runs. Runs P, N, pF'', and nF'' based on the second bred vector were conducted for an auxiliary use in Figs. 9 and 13, thus were not specifically nominated.

3. Analysis method

3.1 Evaluation of nonlinear signal

The nonlinear signals in the initial perturbation growth were evaluated by relative nonlinearity $\Theta(t)$ (Gilmour et al. 2001),

$$\Theta(t) = \frac{\|\boldsymbol{\delta}^{+}(t) + \boldsymbol{\delta}^{-}(t)\|}{0.5(\|\boldsymbol{\delta}^{+}(t)\| + \|\boldsymbol{\delta}^{-}(t)\|)}, \quad (3)$$

where $\|\cdot\|$ denotes an appropriate norm. $\boldsymbol{\delta}^{+}(t)$ and $\boldsymbol{\delta}^{-}(t)$ are the perturbations with each sign at forecast time t; thus, they should initially have the same magnitude and opposite directions, that is, $\boldsymbol{\delta}^{+}(0) = -\boldsymbol{\delta}^{-}(0)$. The relative nonlinearity is zero for perturbation growth in a completely linear system. In a nonlinear system, the relative nonlinearity generally increases to ~1.72 when state vectors $\boldsymbol{\delta}^{+}(t)$ and $\boldsymbol{\delta}^{-}(t)$ have a completely random structure (Hohenegger and Schär 2007b; Appendix A). The maximum relative nonlinearity is 2 when the two perturbations point in the same direction[2].

---

[2] A nonlinear term is a term which consists of two or more products of independent variables, causing a dependent variable unpredictable by a linear relation to independent

Hohenegger and Schär (2007b) prudently introduced relative nonlinearity to indicate the upper-bound time that a tangential linear model accompanying with the forecast model is valid in an operational forecast system. However, the relative nonlinearity calculated with a single pair of initial perturbations is inadequate for assessing the degree of nonlinearity in a system (Gilmour et al. 2001), even among initial perturbations with greatest growth in the model run. This paper only used this metric to diagnose the similarity of state-vector pattens for a particular pair of initial perturbations. The similarity of the perturbation pairs suggests the simulated system's nonlinearity. However, we do not intend to use the value of relative nonlinearity as an index of the degree of atmospheric nonlinearity.

We applied relative nonlinearity to the analysis of a pair of perturbed runs in this

---

variables. A nonlinear dynamical system includes many nonlinear terms in its governing equations like the atmosphere. However, the appearance of nonlinear relation between independent and dependent variables depends on the background state of a dynamical system. This study defines the deviation of the linear relationship between dependent and independent variables as nonlinearity. We quantify this kind of nonlinearity by the relative nonlinearity.

paper. The relative nonlinearity was computed by a perturbation growth vector composed of three-dimensional zonal and meridional wind, potential temperature, water vapor mixing ratio, and surface pressure as $\boldsymbol{\delta}^{\pm}(t) = \left(\delta u^{\pm}\ \delta v^{\pm}\ \delta\theta^{\pm}\ \delta q^{\pm}\ \delta p_s^{\pm}\right)^{\mathbf{T}}$. We formally used the norm of Eq. (1), but the horizontal integration was limited to domain K, fully covering Kyushu Island, Japan (Fig. 2a). The size of the domain K was set to diagnose the relative nonlinearity related to the rainband around Kyushu. The size dependency on domain K was small (see Supplement 1) because the dominant amplitude of perturbations made the main contribution to the relative nonlinearity near the front.

When the relative nonlinearity was also computed for a single variable, the vector components related to the other variables were replaced with zero. For example, the relative nonlinearity for meridional wind was computed by the perturbation growth vector, $\boldsymbol{\delta}^{\pm}(t) = (0\ \delta v^{\pm}\ 0\ 0\ 0)^{\mathbf{T}}$. In another case, the relative nonlinearity for filtered meridional wind was defined as Eq. (3) but with $\boldsymbol{\delta}^{\pm}(t) = \left(0\ \widetilde{\delta v}^{\pm}\ 0\ 0\ 0\right)^{\mathbf{T}}$, where the tilde indicates a filtered variable (Section 3.2).

3.2 Spatial filtering

We applied spatial filtering to the initial perturbations and the resulting forecast fields by a two-dimensional fast Fourier transform (FFT). First, the model domain of 1585 ×

1305 was extended to a domain of 1600 × 1600 by zero padding out of the model domain. This enlarged perturbation field, with zonal and meridional directions widths of *X, Y* = 3198 km, $f(x,y)$, can be expanded as

$$f(x,y) = \sum_{|k| \le K} \sum_{|l| \le L} f_{kl} e^{-ik\frac{2\pi x}{X}} e^{-il\frac{2\pi y}{Y}}, \quad (4)$$

where $K = 1131$ and $L = 1131$ are the wavenumbers (spatial scale at ~3 km) corresponding to the Nyquist frequencies. The low-pass and high-pass filters were designed as the half-amplitude point in weighting coefficient f_{kl} at $k^2 + l^2 = 10^2$ corresponding to the spatial scale at 320 km (see Section 4.2 for the scale selection). The transition band was at wavelengths from 290 to 350 km. The aliasing error was automatically avoided in our analysis because the perturbations were close to zero owing to Rayleigh damping for the same lateral boundary, except for the initial time, in all runs.

To ensure careful treatment in the spatial filtering in our analysis, we applied the Hanning window,

$$W(i) = \frac{1}{2}\left[1 - \cos\left(2\pi \frac{i - 0.5}{N_X}\right)\right], i = 1,2,\ldots N_X, \quad (5)$$

to perturbations before FFT filtering. Here, i is the grid point number and N_X is the number of grid points in the zonal direction. This window was also applied to the perturbation field in the meridional direction. We did not perform preprocessing for detrending because the perturbations have no domain-scale gradient.

4. Results

4.1 Model performance

Initially, we briefly evaluated the performance of JMA's operational model for the target heavy rainfall event comparing the 1-h precipitation rate from run C's 12-h forecast valid at 1800 UTC on 13 August 2021 to the observed precipitation (Fig. 4). A line-shaped rainband was observed over the northern part of Kyushu Island, Japan (Fig. 4a), with the peak precipitation rate exceeding 50 mm h^{-1}. Run C reasonably forecasted this rainband, with a small southwestward bias of about 80 km in the position compared with the observations. Runs P and N also forecasted this rainband, and their forecast difference from run C was large at convective scales.

Related to this rainband, the deep convection line with a width of >20 km was also reproduced by run C, though the position of the line was slightly biased southwestward (Fig. 5). Therefore, we confirmed that the model's control run was able to reproduce the rainband and deep convections in the targeted event.

4.2 Nonlinear perturbation growth

Figure 6 shows the spatial distribution of the perturbation of runs P and N for the meridional wind on the 21st model level (~850 hPa) at forecast times of 2 and 12 h (hereafter, f = X h refers to forecast time at X hours). In both runs, convective-scale perturbation occurred over the rainband, in contrast with the small growth signals over the ocean in the southeast (Figs. 6a,c). The convective-scale perturbation between the runs appeared to be random especially at f = 12 h (Figs. 6b,d), confirming that the spatial correlation between the perturbations in domain K was about 0.4, indicating randomness equivalent to the saturated relative nonlinearity value of 1.72 (Sec 3.1). Runs P and N both developed the same-sign signals for meso-α scale meridional wind perturbation around Kyushu Island: a positive signal over the northern Kyushu area and two negative signals to the northeast and southwest after f = 12 h (white arrows in Figs. 6b,d). This same sign in the perturbation field was a signal of nonlinear perturbation growth reflecting the change in perturbation growth direction in the environment where the midlatitude MCS was observed.

The relative nonlinearity in runs P and N (Fig. 7) increased considerably in the first 2 h of the forecast, corresponding to rapid convective-scale perturbation growth. Thereafter, the relative nonlinearity increased gradually toward the randomness level at ~1.72, consistent with Hohenegger and Schär (2007b). For example, the relative nonlinearity evaluated with selected state-vector components related to meridional wind was close to 1.72 at f = 11 to 13 h, corresponding to a random structure between a pair of runs around Kyushu Island (Figs. 6b,d).

To extract the meso-α scale structure from the perturbation fields, we applied a spatial low-pass filter with a cutoff wavelength of 320 km (the scale selection is explained later in this section) to all perturbation fields for runs P and N (Fig. 8). Focusing on the Kyushu area, the meridional wind perturbation pair has the same sign, with negative patterns over the western sea around Kyushu, positive patterns over Kyushu, and negative patterns over the east of Kyushu. The meridional wind perturbations had similar structures. The perturbation pairs of other variables had the same-sign pattern. For example, the potential temperature perturbation patterns were both positive over Kyushu, but their structures were slightly different. The zonal wind and water vapor perturbation pairs also had similar structures in both perturbations, indicating slightly smaller relative nonlinearity than the meridional wind perturbations.

Temporal evolution of perturbations enabled us to understand how the nonlinear signals emerged and developed (Fig. 9). At the initial time (Fig. 9a), we imposed an absolutely anti-symmetric perturbation between runs P and N. The perturbation magnitudes were small, and the initial perturbation field had a predominant convective-scale component (Fig. 2). In the first 3 h (Figs. 9b–d), linear perturbation growth remained on a scale of more than 320 km. The magnitude increased around the Tsushima Strait between the Korean Peninsula and Kyushu Island only in run P (white arrow in Figs. 9c,d), showing the upscaling of perturbations from the convective to meso-α scales. The perturbations had the same positive signs at *f* = 2 and 3 h (tips of white arrow in Figs. 9c,d) indicating the nonlinear perturbation growth on the line-shaped rainband. However, this same-sign pattern almost disappeared at *f* = 4 h (Fig. 9e), and a sequence of positive/negative perturbations was aligned but the signs of the perturbations were generally opposite in runs P and N (white arrows in Fig. 9e). These patterns moved eastward until *f* = 9 h (Fig. 9j). Meanwhile, the phase pattern in both perturbations shifted with time during *f* = 4 to 9 h (Figs. 9d–j). At *f* = 10 h, these perturbations pointed in the same direction on the line-shaped rainband (white allows in Fig. 9k). This same-sign pattern in both perturbations was stagnant by *f* = 12 h, and the perturbation magnitudes were increased (Figs. 9k–m), as seen in the unfiltered perturbation fields (Figs. 6b,d). This nonlinear signal was also confirmed in another set of runs P and N initialized by the second bred vector (Fig. 9n).

The relative nonlinearity evaluated with selected components of filtered meridional wind perturbations for a pair of runs P and N is shown in Fig. 10. The relative nonlinearity from high-pass-filtered meridional wind perturbations grew rapidly in the first 2 h, regardless of the cutoff wavelength between 20 and 80 km (Fig. 10a). The relative nonlinearity with low-pass-filtered meridional wind perturbation also increased rapidly in the first 2 h (Fig. 10b). This rapid growth corresponded to the nonlinear upscaling seen in Figs. 9c,d. In contrast, the relative nonlinearity based on the low-pass-filtered perturbations of runs P and N was characterized by a gradual increase during f = 4 to 8 h and was almost saturated at the randomness level of ~1.72 around f = 10 h, reflected by the opposite sign of a sequence-like perturbation pattern and its gradual phase shift (Figs. 9d–j). After f = 9 h, the relative nonlinearity with low-pass-filtered perturbations with a cutoff wavelength of 320 km exceeded 1.72, consistent with the same-sign pattern (Figs. 9k–m).

Compared with the relative nonlinearity without the spatial filter, the high-pass filtered relative nonlinearity reached at the randomness level at f = 2 h. On the other hand, the nonfiltered one, which included the mesoscale feature, reached at the randomness level at f = 12 h. These facts showed the transition to a nonlinear regime occurred earlier at small scales, which suggested that the nonlinear signals of the perturbation were upscaled from the convective scale (Fig. 9c). This may be related to the meso-α scale structure with the same-sign perturbations near the rainband at f = 10 h in runs P and N (Fig. 9k). The relative nonlinearity was high at the cutoff wavelength of 320 km (Fig. 10b).

This is the reason why we selected 320 km as the cutoff wavelength for the spatial filtering.

4.3 Origin of the upscaling process and the nonlinear signals

In the previous subsection, we found nonlinear signals with a high relative nonlinearity on a scale of more than 320 km related to the upscaling from convective scales around the active convection area. However, it is difficult to investigate the origin of nonlinear signals in widespread, complex, multiscale MCSs even by the animating the time evolution of the meridional wind perturbation (Supplement 2). We therefore examined the initial perturbation sensitivity to the nonlinear signals around the line-shaped rainband in runs P and N (Fig. 9) by performing additional runs with an initial patch perturbation (Table 1). The origin of the upscaling process can be identified by the contribution of the patch perturbation to the nonlinear signals in runs P and N. The sensitivity of the perturbed variables and moist physics to the nonlinear signals and the upscaling process was also investigated.

a. Sensitivity to the initial perturbation regions

In the additional runs, we trimmed the initial perturbations based on bred vectors within a radius of 40 km from a point at the stationary front or its southern side (Figs. 11a,c,e,g,i). We chose 40 km as the perturbation patch size because it exceeds the smallest scale of a convection that the forecast model can represent sufficiently. The patch size sensitivity to nonlinear signals will be reported elsewhere.

Runs pF and nF reproduced the positive sign over Kyushu and negative signs over the areas on each side (Fig. 11b), but the phases between the positive and negative perturbations were slightly different. Runs pF’ and nF’, in which the perturbation was introduced near the rainband, also reproduced similar nonlinear signals, although the signals were located in the downstream region of the rainband (Fig. 11d, white arrows). Runs pF’’ and nF’’, in which double patches were imposed as the initial perturbations, reproduced the positive sign over northern Kyushu Island and negative signs over the areas on each side (Fig. 11f) better than any other pair of runs. Runs pF, nF, pF’, nF’, pF’’ and nF’’ indicated that the nonlinear signals observed at f = 12 h originated from the initial perturbations in the upstream region of the line-shaped rainband on the stationary front where the convection was active. The perturbation out from the stationary front was ineffective in producing the nonlinear signals around Kyushu; runs pS and nS and runs pS’ and nS’, in which the southern regions of the stationary front were initially perturbed, did not generate strong nonlinear signals (Figs. 11h,j).

Figure 12 shows the relative nonlinearity of the low-pass-filtered meridional wind perturbations for additional experiments. Runs pF'' and nF'' showed that the relative nonlinearity rapidly increased in the first 2 h, slightly decreased, and increased again after 5 h, similar to the features of runs P and N. Runs pS, nS, pS' and nS' did not reproduce this rapid increase in the relative nonlinearity. The second peak in runs pF'' and nF'' occurred at *f* = 11 h, almost at the same timing as that in runs P and N (around *f* = 12 h). The time evolution of the relative nonlinearity from runs pF'' and nF'' was closest to that from runs P and N.

We also confirmed the similarity of runs pF'' and nF'' to runs P and N from the time evolution of the horizontal distribution (Fig. 13), that is, the upscaling signal at *f* = 2 h (Fig. 13c), the linear perturbation patterns at *f* = 4 to 9 h (Figs. 13e–j), and the nonlinear pattern after *f* = 10 h (Figs. 13k–m). This nonlinear signal was also seen in additional runs pF'' and nF'', initialized by the second bred vector (Fig. 13n). Considering that runs pF'' and nF'' provided a similar nonlinear signal to runs P and N, and not to other pairs, we explored the origin of the nonlinear signals at the stationary fronts with runs pF'' and nF''.

b. Origin of the upscaling process

We analyzed the results for runs pF'' and nF'' by zooming into the region around the origin of the nonlinear signals to investigate the upscaling process from the convective scale to the meso-α scale. We restored the perturbation fields with no spatial filtering to observe all scales resolved in the model. Figure 14 shows the time evolution of the meridional wind perturbation around the initially perturbed region in runs pF'' and nF''. The opposite sign patterns, positive in run pF'' and negative in run nF'' (green arrows in Fig. 14), moved eastward and expanded with time. These perturbation patterns indicated the linear upscaling of the perturbations (white arrows in Fig. 13e).

On the other hand, both runs pF'' and nF'' have a positive signal to the south of the rainband (white arrow in Fig. 14b,c,f,g), suggesting a nonlinear growth of the perturbation. These same-sign patterns might contribute to the increase of relative nonlinearity at f = 2–3 h (Fig. 12). The southeastern tip of the positive signal moved ~ 90 km from f = 2 to 3 h in runs pF'' and nF'' (Figs. 14b,c,f,g), indicating that the propagation speed was about 90 km h^{-1}. We estimated the propagation speed of a gravity wave following Selz and Craig (2015). The hydrostatic nonrotating regime yielded the gravity wave speed as the Brunt–Väisälä frequency divided by the vertical wavenumber (Gill 1982). Because the vertical wavenumber was 1 at the tropospheric depth (15 km; not shown) and the Brunt–Väisälä frequency was 0.01 s^{-1} at f = 2 h in domain K, the gravity wave speed was 86 km h^{-1}, suggesting that perturbations were propagated outwards by the gravity wave. These results implied that the gravity waves excited in convective areas were a source of upscaling to the nonlinear perturbation patterns.

c. Origin of the nonlinear signals

The same-sign patterns, positive in both runs, moved eastward after *f* = 1 h (white arrows in Figs. 14a-c,e-g). This pattern corresponded to the nonlinear signal on the meso-α scale (Fig. 13c) and the first increase in the relative nonlinearity at *f* = 2 h (Fig. 12). This nonlinear signal dissipated after *f* = 2 h, and instead, the opposite-sign perturbations prevailed, corresponding to an intermittent decrease in the relative nonlinearity by *f* = 4 h (Fig. 12). After then, the same positive-sign perturbation (white arrows in Fig. 15) was westward of the opposite-sign perturbations after *f* = 5 h. The same negative-sign perturbation was also found after *f* = 9 h. These nonlinear signals expanded from southwest to northeast at *f* = 11 h. The dominance of these nonlinear signals contributed to the second gradual increase in the relative nonlinearity by *f* = 11 h (Fig. 12).

Figure 16 shows the power spectra of meridional wind perturbation in run pF'' (Fig. 16a) and the ratio of the meridional wind perturbation power spectra for the sum of the perturbations in runs pF'' and nF'' and the double-amplitude perturbation in run pF'' (Fig. 16b). Because this sum was the numerator in Eq. (3), its non-zero value was the nonlinear component represented by the perturbations in runs pF'' and nF''. A ratio value of 1 means that the amplitude of the nonlinear signal is equivalent to twice the amplitude of run pF''.

The perturbation growth of run pF'' was significant on a horizontal scale smaller than 40 km during the first 1 h (red arrow in Fig. 16a), indicating the rapid convective-scale perturbation growth. The perturbation on a scale larger than 200 km grew at the same time, showing the mesoscale perturbations were related to the gravity wave propagation. The power ratio also increased rapidly on a scale smaller than 40 km during the first 1 h (Fig. 16b). After 1 h, perturbation growth occurred at all scales (Fig. 16a). The power ratio increased greatly at all scales until 2 h (Fig. 16b). The meso-scale nonlinear signal on a scale larger than 100 km fluctuated after f = 2 h, whereas the nonlinear signals on a scale smaller than 100 km attained the saturated value of 0.7–0.8 (Fig. 16b). The peak power ratios at f = 2 and 3 h, corresponding to a 100 km wavelength, reflected the nonlinear signals in Figs. 14b,c,f,g. The power ratio eventually reached the saturated value of 0.7–0.8 at f = 12 h on a scale smaller than 300 km, which reflected the strengthening of the nonlinear signals at the meso-α scale (Figs. 13k–m). The power spectrum diagnosis for the sum of runs pF'' and nF'' indicated a clear upscaling of the nonlinear signals, which shows the changes in error growth direction, simulated in our experiment.

d. Sensitivities of variables and moist physics

Additional experiments with trimmed perturbations same as pF'' and nF'' but restricted further to wind, temperature, or water vapor (Fig. 17) revealed a contribution comparable to the results above. The low-pass-filtered meridional wind perturbations showed that runs with temperature and water vapor perturbation (Figs. 17b,c) corresponded to runs pF'' and nF'' (Fig. 13m). The relative nonlinearities from runs pT and nT and runs pQ and nQ increased rapidly by *f* = 2 h (Fig. 18), which indicated that the initial perturbations in the potential temperature or water vapor may contribute to the rapid upscaling related to moist convection. In contrast, the runs with wind perturbation less showed nonlinear signals at *f* = 12 h (Fig. 17a). However, the relative nonlinearity in runs pW and nW reached its peak in the later stage at *f* = 14 h (Fig. 18). Therefore, wind also contributed to the nonlinear signals on the meso-α scale.

Finally, we performed runs pD and nD without the convective parameterization and the cloud microphysics during the model integrations. The signal at *f* = 12h was almost linear and its amplitude was small compared with the other runs (Fig. 17d). A slight upscaling process was detected in the beginning of the forecast time but was likely independent of the convective activities (not shown). The relative nonlinearity remained smaller than in the other run pairs. This supported the idea that the moist physics in the forecasting model was essential for generating nonlinear signals in the convective area.

5. Conclusion and discussion

We assessed the nonlinearity of an MCS by analyzing the growth direction of perturbation pairs with initially opposite sign and the nonlinear signal at both convective and mesoscales to see if there was an upscaling feature. First, we confirmed that the forecast perturbation had the same-signed meso-α scale nonlinear signals that expanded from the center of the rainband. The relative nonlinearity was high after a few forecast hours at both convective scales and mesoscale. The additional experiments revealed that the nonlinear signals were originated from the gravity waves emitted from the rainbands in a few hours from the initial forecast time. The nonlinear signal at mesoscale was also confirmed around f = 10 h. These nonlinear signals on the meso-α scale did not appear from the experiment without the moist physics. These results indicated the importance of upscaling from a MCS through moist convections for the nonlinear meso-α scale perturbation patterns. This study sheds new light on atmospheric nonlinearity by demonstrating the upscaling aspect of the change in the direction of error growth.

This study showed the generation of nonlinear signals near a horizonal shear zone on the stationary front, as identified by the relative nonlinearity. The almost-saturated environment that we targeted in this study made the nonlinear response sensitive to when and where moist convective cells built up. A moisture or low-pressure perturbation may have triggered or suppressed convective cells at those locations. Regardless of the signal sign, this possibly resulted in a different density-surface uplifting in the convective timescales compared with the control run. Although runs pD and nD demonstrated that moist physics was essential for the nonlinear signals, the generation process of the nonlinear perturbation pattern in the convective areas remained unclear and requires further research.

Although this study only focused on the single MCS case in western Japan, the knowledge that we obtained could be applied to other cases in which an environment appears repeatedly in an Asian summer monsoonal season. Such environment often induces an organized convective activity. The nonlinear response could also be detected in moving disturbances such as squall lines and supercells associated with baroclinic waves, because the convective area is almost saturated in the horizontal shear zone. However, the perturbation changes should depend on the advection in the moving disturbances, which is beyond the scope of this study.

In contrast to MCSs, it is expected that scattered thunderstorms would not show a nonlinear response on the meso-α scale because the convection is disorganized. In future work, our findings could be applied to other convective systems.

Data Availability Statement

The programing code including the numerical forecast model used in this study and the calculation results cannot be provided due to JMA's policy. They will be made available upon consultation. The initial and lateral boundary conditions used in this study can be purchased from the Japan Meteorological Business Support Center.

Supplement

Supplement 1 shows relative nonlinearity as a function of forecast time (h) between the 16th and 26th model levels. Calculated in (black) domain K (Fig. 2a), (green) whole forecast domain, (red) domain within 27.5°N to 37.5°N and 125°E to 135°E, and (yellow) domain within 30°N to 35°N and 127.5°E to 132.5°E.

Supplement 2 shows an animation of perturbations of meridional wind (m s^{-1}) on the 21st model level (~850 hPa) in runs pF until f = 12 h.

Acknowledgments

We would like to thank the Editor and two anonymous reviewers to provide constructive comments that helped us improve the manuscript. We also thank Dr. Hiroaki Miura of the University of Tokyo for his insightful comments on our preliminary results. KO was supported by JSPS KAKENHI Grant Number 23K03498. MI was supported by the Advanced Studies of Climate Change Projection (SENTAN) Grant Number JPMXD0722680734 of the Ministry of Education, Culture, Sports, Science, and Technology, Japan; and by Research Field of Hokkaido Weather Forecast and Technology Development (endowed by Hokkaido Weather Technology Center Co., Ltd.).

Appendix A

The relative nonlinearity for two pairs of random vectors of ~1.72 is described here. First, we introduce a Gaussian distribution with a mean of 0 and standard deviation σ,

$$N(0,\sigma) = \frac{1}{\sqrt{2\pi}\sigma}\exp\left(-\frac{x^2}{2\sigma^2}\right), \tag{A1}$$

and the χ^2 distributions with 1 degree of freedom,

$$\chi^2(1) = \frac{1}{\sqrt{2\pi x}}\ \exp\left(-\frac{x}{2}\right). \tag{A2}$$

Let x and y be an element of n-dimensional state vectors $\boldsymbol{x}$ and $\boldsymbol{y}$ followed by Gaussian distributions $N(0,a)$ and $N(0,b)$, respectively. Here, standard deviations a and b are followed by $\chi^2(1)$. Given a and b, the numerator of the relative nonlinearity for two random vectors [Eq. (3)] is the norm of two vectors, which is equivalent to the square of the sum of two random numbers estimated by the expectation value of $(x+y)^2$,

$$\int_{\mathbb{R}^2} (x+y)^2 \frac{1}{\sqrt{2\pi a}} \exp\left(-\frac{x^2}{2a^2}\right) \frac{1}{\sqrt{2\pi b}} \exp\left(-\frac{y^2}{2b^2}\right) dxdy = a^2 + b^2 \quad \text{(A3)}$$

The expectation value of $\|\boldsymbol{x}+\boldsymbol{y}\|^2$ is the n sum of a^2+b^2. Factor n is also in denominator $\|\boldsymbol{x}\|^2$ and $\|\boldsymbol{y}\|^2$ of the relative nonlinearity, and thus n is canceled out. Then, the expectation value of $\|\boldsymbol{x}+\boldsymbol{y}\|$ is

$$\mathbb{E}\left[\sqrt{a^2+b^2}\right] = \int_0^\infty \int_0^\infty \sqrt{a^2+b^2} \frac{1}{\sqrt{2\pi a}} e^{-\frac{a}{2}} \frac{1}{\sqrt{2\pi b}} e^{-\frac{b}{2}} dadb \sim 1.71969, \quad \text{(A4)}$$

which is nearly $\sqrt{3} \sim 1.73205$ (Hohenegger and Schär 2007a).

References

Beljaars, A. C. M., and A. A. M. Holtslag, 1991: Flux parameterization over land surfaces for atmospheric models. *J. Appl. Meteor.*, **30**, 327–341. https://doi.org/10.1175/1520-0450(1991)030<0327:FPOLSF>2.0.CO;2

Bierdel, L., T. Selz, and G. Craig, 2017: Theoretical aspects of upscale error growth through the mesoscales: An analytical model. *Quart. J. Roy. Meteor. Soc.*, **143**, 3048–3059. https://doi.org/10.1002/qj.3160.

Bierdel, L., T. Selz, and G. C. Craig, 2018: Theoretical aspects of upscale error growth on the mesoscales: Idealised numerical simulations. *Quart. J. Roy. Meteor. Soc.*, **144**, 682–694. https://doi.org/10.1002/qj.3236.

Bluestein, H. B., and M. H. Jain, 1985: Formation of mesoscale lines of precipitation: Severe squall lines in Oklahoma during the spring. J. Atmos. Sci., 42, 1711–1732. https://doi.org/10.1175/1520-0469(1985)042%3C1711:FOMLOP%3E2.0.CO;2

Durran, D. R., and J. A. Weyn, 2016: Thunderstorms do not get butterflies. *Bull. Amer. Meteor. Soc.*, **97**, 237–243, https://doi.org/10.1175/BAMS-D-15-00070.1.

Ehrendorfer, M., R. M. Errico, and K. D. Raeder, 1999: Singular-vector perturbation growth in a primitive equation model with moist physics. *J. Atmos. Sci.*, **56**, 1627–1648.

Gill, A.E., 1982: Atmosphere-ocean dynamics. Academic Press, 680pp.

Gilmour, I., L. A. Smith, and R. Buizza, 2001: Linear regime duration: Is 24 hours a long time in synoptic weather forecasting? *J. Atmos. Sci.*, **58**, 3525–3539. https://doi.org/10.1175/1520-0469(2001)058<3525:LRDIHA>2.0.CO;2.

Hara, T., 2015: Necessity of parameterizations for convective initiation in high resolution cloud-permitting models. *CAS/JSC WGNE Res. Activ. Atmos. Oceanic Modell.*, **45**, 04.06–04.07.

Hirockawa, Y., T. Kato, H. Tsuguti, and N. Seino, 2020: Identification and classification of heavy rainfall areas and their characteristic features in Japan. *J. Meteor. Soc. Japan*, **98**, 835−857. https://doi.org/10.2151/jmsj.2020-043.

Hohenegger, C., and C. Schär, 2007a: Predictability and error growth dynamics in cloud-resolving models. *J. Atmos. Sci.*, **64**, 4467–4478. https://doi.org/10.1175/2007JAS2143.1

Hohenegger, C., and C. Schär. 2007b: Atmospheric predictability at synoptic versus cloud-resolving scales. *Bull. Amer. Meteor. Soc.*, **88**, 1783–1793. https://doi.org/10.1175/BAMS-88-11-1783.

Ikuta, Y., T. Fujita, Y. Ota, and Y. Honda, 2021: Variational data assimilation system for operational regional models at Japan meteorological agency. *J. Meteor. Soc. Japan*, **99**, 1563-1592. https://doi.org/10.2151/jmsj.2021-076.

Ishida, J., K. Aranami, K. Kawano, K. Matsubayashi, Y. Kitamura, and C. Muroi, 2022: ASUCA: the JMA operational non-hydrostatic model. *J. Meteor. Soc. Japan*, **100**, 825–846. https://doi.org/10.2151/jmsj.2022-043.

Japan Meteorological Agency, 2022: Outline of the operational numerical weather prediction at the Japan Meteorological Agency. Appendix to WMO Tech. Progress Rep. on the Global Data-processing and Forecasting System and Numerical Weather Prediction, Tokyo, Japan Meteorological Agency, accessed 20 May 2024 [Available at https://www.jma.go.jp/jma/jma-eng/jma-center/nwp/outline2022-nwp/index.htm]

Kain, J. S., and J. M. Fritsch, 1990: A one-dimensional entraining/detraining plume model and its application in convective parameterization. *J. Atmos. Sci.*, **47**, 2784–2802. https://doi.org/10.1175/1520-0469(1990)047<2784:AODEPM>2.0.CO;2.

Kato, T., 2020: Quasi-stationary band-shaped precipitation systems, named “senjo-kousuitai,” causing localized heavy rainfall in Japan. *J. Meteor. Soc. Japan*, **98**, 485–509. https://doi.org/10.2151/jmsj.2020-029.

Kawano, T., and R. Kawamura, 2020: Genesis and maintenance processes of a quasi-stationary convective band that produced record-breaking precipitation in northern Kyushu, Japan on 5 July 2017. *J. Meteor. Soc. Japan*, **98**, 673−690. https://doi.org/10.2151/jmsj.2020-033.

Kühnlein, C., C. Keil, G. C. Craig, and C. Gebhardt, 2014: The impact of downscaled initial condition perturbations on convective-scale ensemble forecasts of precipitation. *Quart. J. Roy. Meteor. Soc.*, **140**, 1552–1562. https://doi.org/10.1002/qj.2238.

Lin, Y., 2006: Mesoscale Dynamics. Cambridge University Press, 630 pp.

Minamide, M., F. Zhang, and E. E. Clothiaux, 2020: Nonlinear forecast error growth of rapidly intensifying Hurricane Harvey (2017) examined through convection-permitting ensemble assimilation of GOES-16 all-sky radiances. *J. Atmos. Sci.*, **77**, 4277–4296. https://doi.org/10.1175/JAS-D-19-0279.1.

Nakanishi, M., and H. Niino, 2009: Development of an improved turbulence closure model for the atmospheric boundary layer. *J. Meteor. Soc. Japan*, **87**, 895–912. https://doi.org/10.2151/jmsj.87.895.

Ono, K., M. Kunii, and Y. Honda, 2021: The regional model-based Mesoscale Ensemble Prediction System, MEPS, at the Japan Meteorological Agency. *Quart. J. Roy. Meteor. Soc.*, **147**, 465–484. https://doi.org/10.1002/qj.3928.

Raynaud, L., and F. Bouttier, 2017: The impact of horizontal resolution and ensemble size for convective-scale probabilistic forecasts. *Quart. J. Roy. Meteor. Soc.*, **143**, 3037–3047. https://doi.org/10.1002/qj.3159.

Rodwell, M. J., and Coauthors, 2013: Characteristics of occasional poor medium-range weather forecasts for Europe. *Bull. Amer. Meteor. Soc.*, **94**, 1393–1405. https://doi.org/10.1175/BAMS-D-12-00099.1

Selz, T., and G. C. Craig, 2015: Upscale error growth in a high-resolution simulation of a summertime weather event over Europe. *Mon. Wea. Rev.*, **143**, 813–827. https://doi.org/10.1175/MWR-D-14-00140.1.

Sun, Y. Q., and F. Zhang, 2016: Intrinsic versus practical limits of atmospheric predictability and the significance of the butterfly effect. *J. Atmos. Sci.*, **73**, 1419–1438. https://doi.org/10.1175/JAS-D-15-0142.1.

Toth, Z., and E. Kalnay, 1993: Ensemble forecasting at NMC: The generation of perturbation. *Bull. Amer. Meteor. Soc.*, **74**, 2317–2330. doi:10.1175/1520-0477(1993)074,2317:EFANTG.2.0.CO;2.

Wang, Y., M. Bellus, J.-F. Geleyn, X. Ma, W. Tian, and F. Weidle, 2014: A new method for generating initial condition perturbations in a regional ensemble prediction system: blending. *Mon. Wea. Rev.*, **142**, 2043–2059. https://doi.org/10.1175/MWR-D-12-00354.1.

Weyn, J. A., and D. R. Durran, 2017: The dependence of the predictability of mesoscale convective systems on the horizontal scale and amplitude of initial errors in idealized simulations. *J. Atmos. Sci.*, **74**, 2191–2210. https://doi.org/10.1175/JAS-D-17-0006.1.

Wu, P.-Y., and T. Takemi, 2023: Impacts of mountain topography and background flow conditions on the predictability of thermally induced thunderstorms and the associated error growth. *J. Atmos. Sci.*, **80**, 1177–1199. https://doi.org/10.1175/JAS-D-21-0331.1.

Zhang, F., N. Bei, R. Rotunno, C. Snyder, and C. C. Epifanio, 2007: Mesoscale predictability of moist baroclinic waves: convection-permitting experiments and multistage error growth dynamics. *J. Atmos. Sci.*, **64**, 3579–3594. https://doi.org/10.1175/JAS4028.1.

List of Figures

between black dotted lines is Kyushu. (c) Same as (b), but for the run C at *f* = 12 h.

Fig. 6 (a,b) Meridional wind perturbation (m s^{-1}) on the 21st model level (~850 hPa) in run P at (a) *f* = 2 h and (b) *f* = 12 h. The range between −0.1 and 0.1 is white. White open arrows in (b) help to explain the nonlinearity in the text. (c,d) Same as (a,b), but for run N.

Fig. 7 Relative nonlinearity for all variables and each variable calculated between the 16th and 26th model levels (approximately between 900 and 2200 m). The dotted horizontal line denotes the relative nonlinearity value of ~1.72.

Fig. 8 Low-pass-filtered perturbations of (a) zonal wind (m s^{-1}), (b) meridional wind (m s^{-1}), (c) potential temperature (K), and (d) water vapor (g kg^{-1}) on the 21st model level at *f* = 12 h in (color shades) run P and (contours) run N. The color shades are partially log-scaled as per the reference in the bottom. The range between −0.1 and 0.1 is white for run P. The contour levels are 0.0, ±0.1, ±0.2, ±0.4, ±0.8, ±1.6, and ±3.2, with negative contours dashed. The green line shows Kyushu Island. The yellow line is the contour line for precipitation forecasted by run C of 10 mm h^{-1}, including areas exceeding 50 mm h^{-1}. Values on each panel are the relative nonlinearity for each variable calculated between the 16th and 26th model levels (approximately between 900 and 2200 m).

Fig. 9 Low-pass-filtered meridional wind perturbation (m s^{-1}) on the 21st model level from (a)−(m) *f* = 0 to 12 h in (color shades) run P and (contours) run N. (n) Same as (m), but based on the second bred vector. The range between −0.1 and 0.1 is white for run P. The white arrows in (c,d,e,k) are to help the explanations in the text. The yellow line is the contour line for precipitation forecasted by run C of 10 mm h^{-1}, including areas exceeding 50 mm h^{-1}.

Fig. 10 Relative nonlinearity for (a) high-pass and (b) low-pass-filtered meridional wind perturbation calculated between the 16th and 26th model levels. The dotted horizontal line denotes the relative nonlinearity value of ~1.72.

Fig. 11 (a,c,e,g,i) Meridional wind perturbation (m s^{-1}) on the 21st model level at the initial time for runs (a) pF, (c) pF’, (e) pF’’, (g) pS, and (i) pS’. (b,d,f,h,j) Meridional wind perturbation (m s^{-1}) on the 21st model level with low-pass spatial filtering with a cutoff wavelength of 320 km at *f* = 12 h for runs (b) pF and nF, (d) pF’ and nF’, (f) pF’’ and nF’’, (h) pS and nS, and (j) pS’ and nS’. Solid lines indicate positive values and dotted lines indicate negative values with intervals of 0.0, $\pm$0.1, $\pm$0.2, $\pm$0.4, $\pm$0.8, $\pm$1.6, and $\pm$3.2 in runs nF, nF’, nF’’, nS, and nS’. The yellow line is the contour line for precipitation forecasted by run C of 10 mm h^{-1}, including areas exceeding 50 mm h^{-1}. The green line shows Kyushu island. The white arrows in (d) are to help the explanations in the text.

Fig. 12 Relative nonlinearity as a function of forecast time (h) for low-pass-filtered meridional wind perturbations calculated between the 16th and 26th model levels for pairs of runs (black) P and N, (yellow) pF and nF, (orange) pF’ and nF’, (red) pF’’ and nF’’, (blue) pS and nS, and (skyblue) pS’ and nS’. The dotted horizontal line denotes the relative nonlinearity value of ~1.72.

Fig. 13 Same as Fig. 9, but for runs pF’’ and nF’’. Green boxes show the close-up region in Figs. 14 and 15.

Fig. 14 Meridional wind perturbation (m s^{-1}) on the 21st model level at *f* = 1 to 4 h in run pF’’ (a−d) and nF’’ (e−h). The green and white arrows are to help the explanations in the text for linear and nonlinear signals, respectively. The black broken lines in (b and f) shows the tip of the positive values at *f* = 2 h. The black broken lines in (c and

g) show the tips at f = 2 and 3 h. The yellow line shows the contour line for precipitation forecasted by run C of 10 mm h^{-1}, including areas exceeding 50 mm h^{-1}.

Fig. 15 Same as Fig. 14, but at f = 5, 7, 9, and 11 h.

Fig. 16 Power spectra of meridional wind perturbation in (a) run pF'' and (b) ratio of between the power spectra of sum of runs pF'' and nF'' and of run pF'' with double amplitude at f = (black) 0, (skyblue) 1, (purple) 2, (green) 3, (yellow) 6, (orange) 12, and (red) 18 h. Black line denotes the −5/3 power law as a reference. The red arrow is to help the explanation in the text.

Fig. 17 Low-pass-filtered meridional wind perturbation (m s^{-1}) on the 21st model level at f = 12 h for pairs of runs (a) pW and nW, (b) pT and nT, (c) pQ and nQ, and (d) pD and nD.

Fig. 18 Relative nonlinearity as a function of forecast time (h) for low-pass filtered meridional wind perturbations calculated between the 16th and 26th model levels for pairs of runs (red) pF'' and nF'', (green) pW and nW, (yellow) pT and nT, (skyblue) pQ and nQ, and (black) pD and nD.

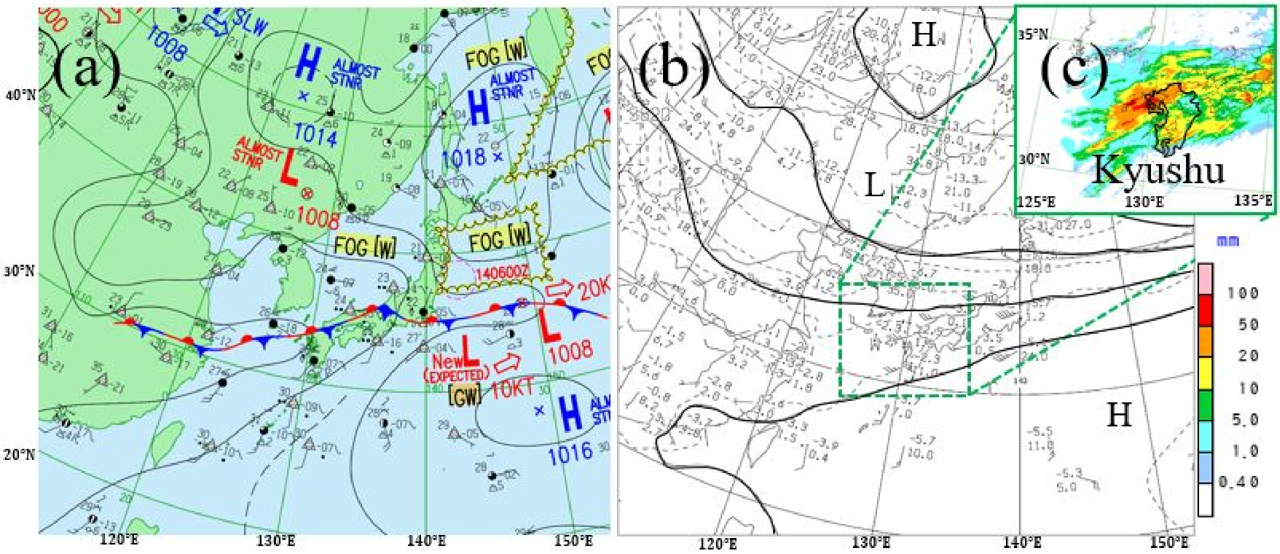

Fig. 1 (a) Japan Meteorological Agency (JMA) surface weather chart and (c) 3-h accumulated precipitation observed by Radar/Raingauge-Analyzed Precipitation data (R/A: JMA 2022) at 0600 UTC on 13 August 2021. (b) JMA 500 hPa weather chart at 0000 UTC on 13 August 2021 showing geopotential height (black contours). In (c), the color shading is as per the reference in the right panel and the bold black line shows Kyushu Island.

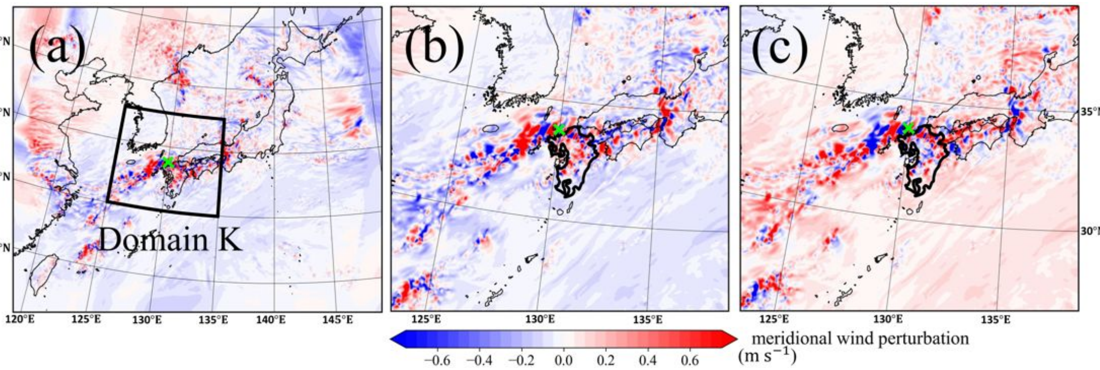

Fig. 2 (a) Initial perturbations of meridional wind (m s^{-1}) on the 21st model level (~850 hPa) at 0600 UTC on 13 August 2021. The color scale is shown at the bottom of the figure. The area enclosed by the black line is domain K, used in the calculation of relative nonlinearity (Section 3.1). (b) Enlarged view of Kyushu Island in (a), not the same as domain K. (c) Same as (b), but for the opposite sign for the negative run (see Section 2.3). The green cross indicates the center of domain K.

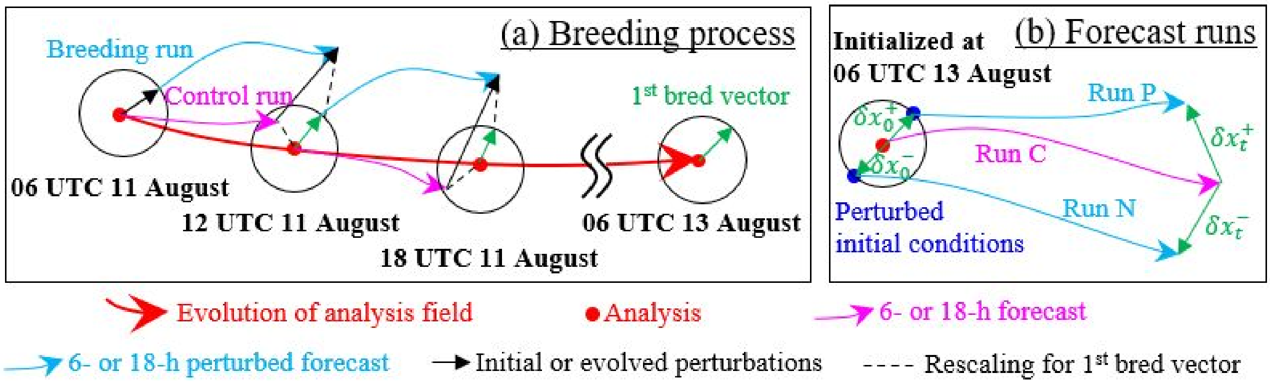

Fig. 3 Schematics of the (a) breeding process and (b) control and perturbed forecasts. Green arrows in (a) are bred vectors, and the first bred vector in (a) was used in the perturbed runs in (b).

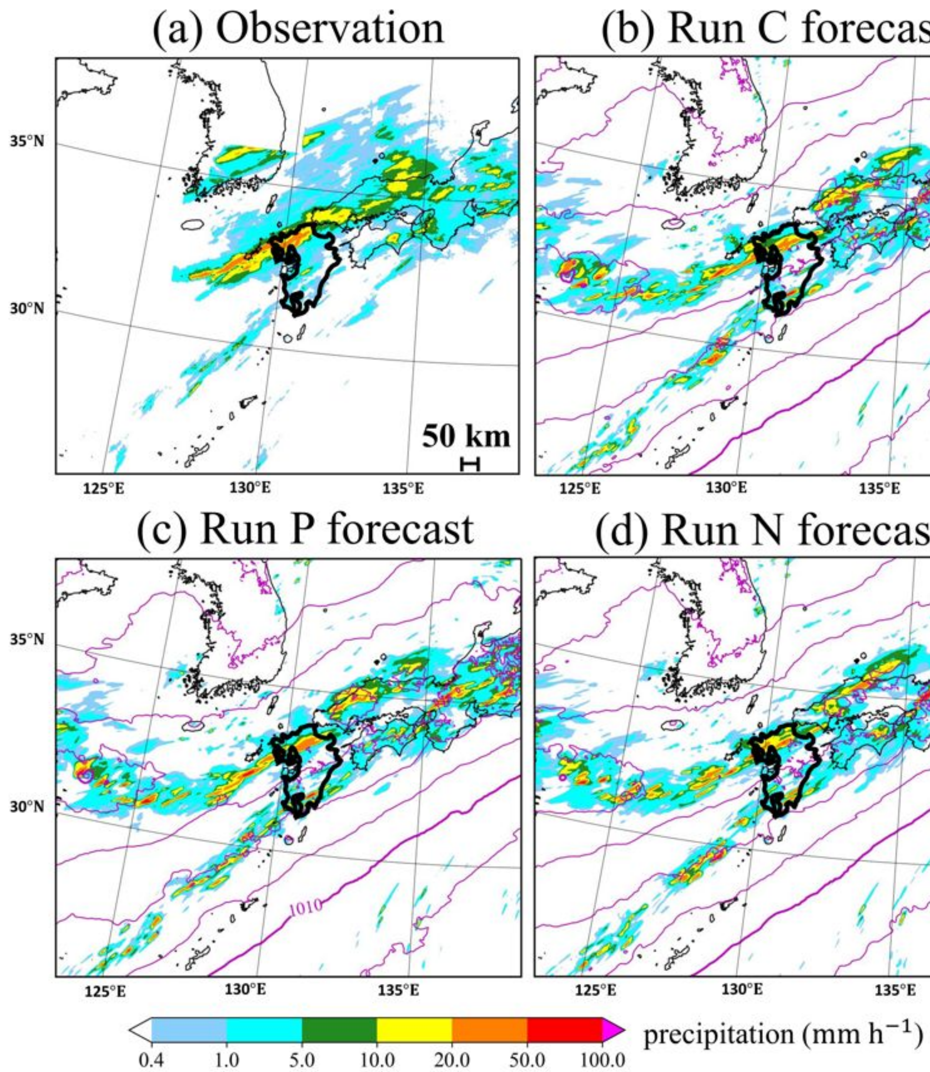

Fig. 4 One-hour accumulated precipitation (mm h^{-1}) around Kyushu Island, Japan at 1800 UTC on 13 August 2021 for (a) the R/A observation and (b,c,d) runs C, P, and N at *f* = 12 h. The color scale is shown at the bottom. In (b,c,d), the mean sea level pressure is superimposed as magenta contours with an interval of 2 hPa.

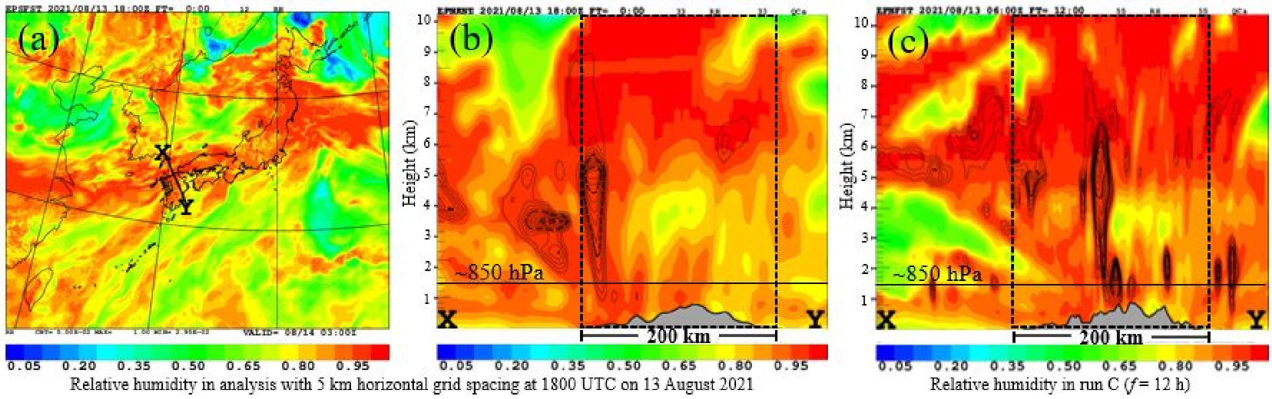

Fig. 5 (a) Relative humidity at the 21st model layer (~850 hPa) from the analysis with a 5km grid spacing at 1800 UTC on 13 August 2021. (b) Vertical cross section of relative humidity along the line segment X to Y in (a). Cloud water is superimposed as black contours with an interval of 0.1 g kg^{-1} in (b) and (c). The region sandwiched between black dotted lines is Kyushu. (c) Same as (b), but for the run C at f = 12 h.

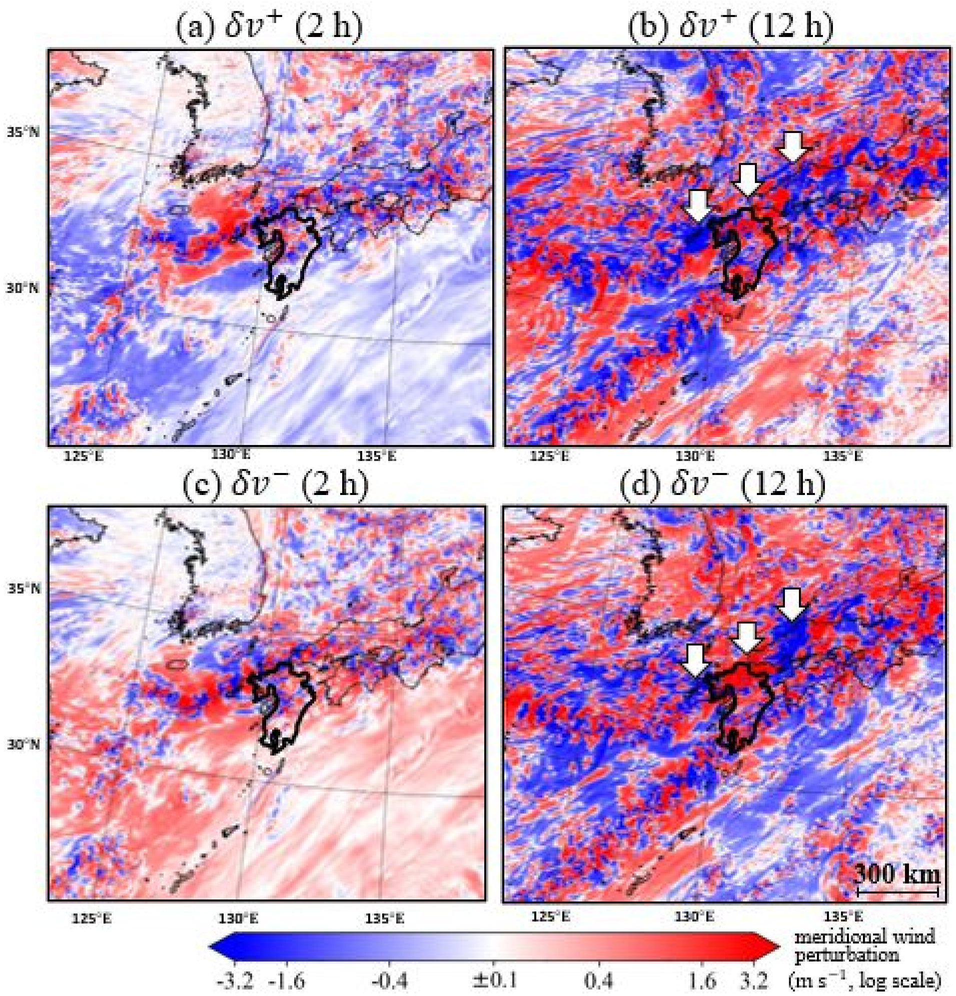

Fig. 6 (a,b) Meridional wind perturbation (m s^{-1}) on the 21st model level (~850 hPa) in run P at (a) f = 2 h and (b) f = 12 h. The range between −0.1 and 0.1 is white. White open arrows in (b) help to explain the nonlinearity in the text. (c,d) Same as (a,b), but for run N.

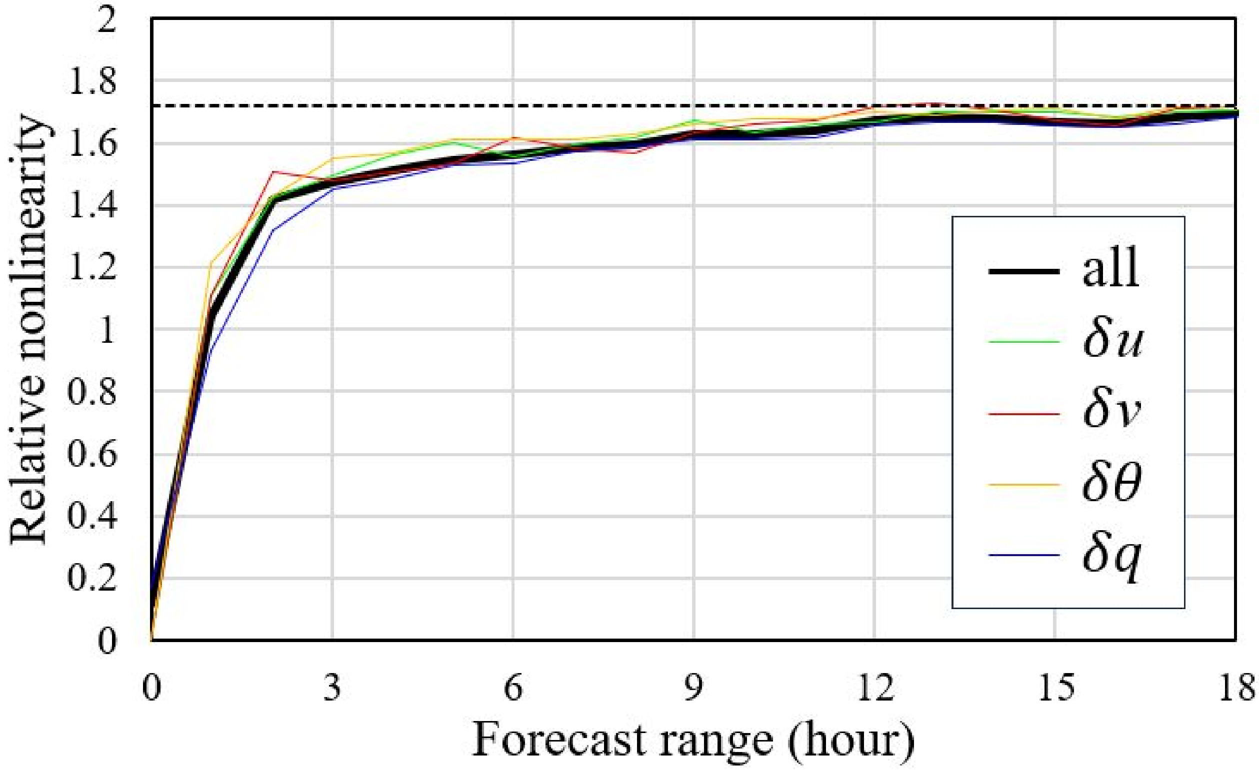

Fig. 7 Relative nonlinearity for all variables and each variable calculated between the 16th and 26th model levels (approximately between 900 and 2200 m). The dotted horizontal line denotes the relative nonlinearity value of ~1.72.

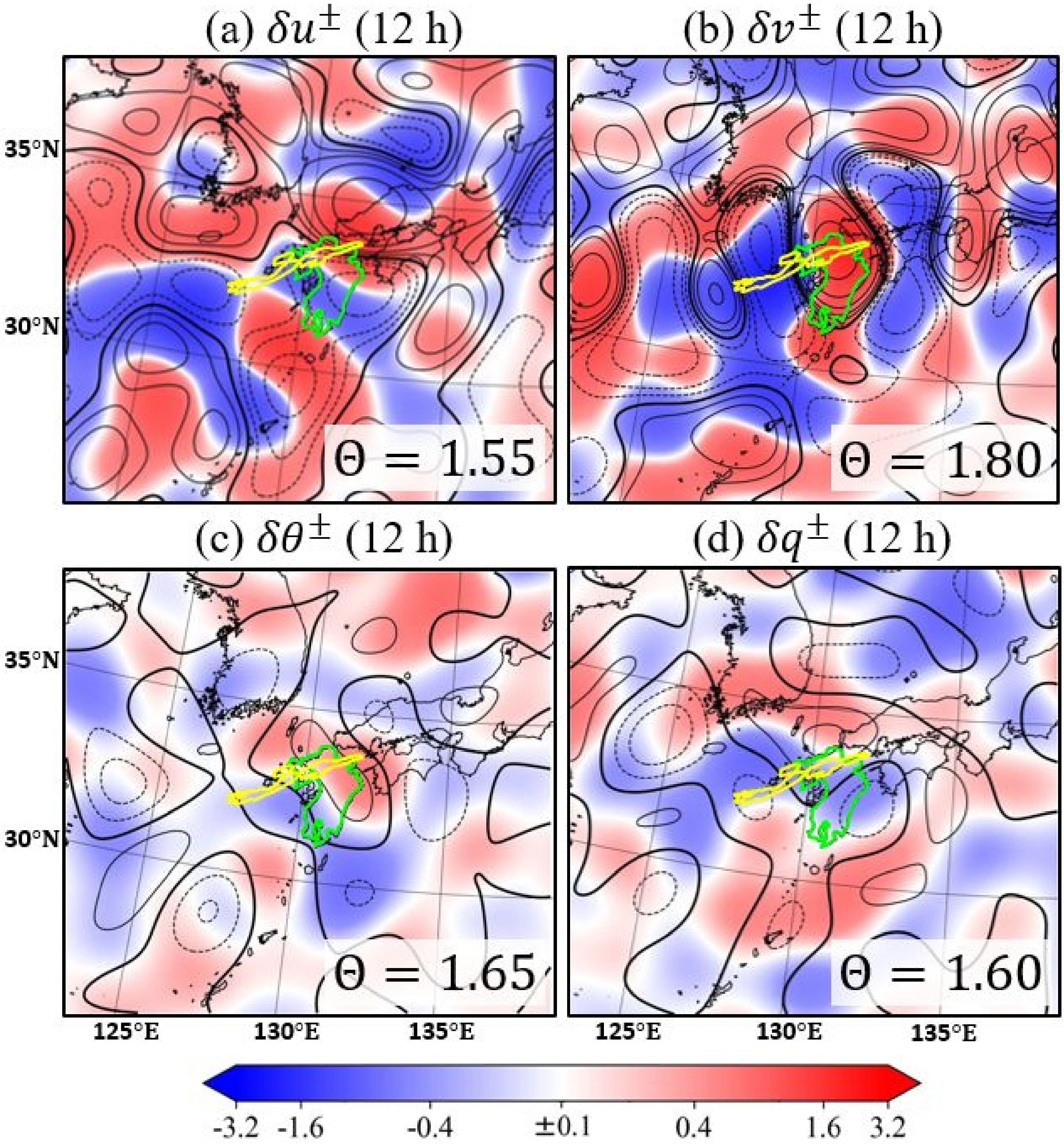

Fig. 8 Low-pass-filtered perturbations of (a) zonal wind (m s^{-1}), (b) meridional wind (m s^{-1}), (c) potential temperature (K), and (d) water vapor (g kg^{-1}) on the 21st model level at f = 12 h in (color shades) run P and (contours) run N. The color shades are partially log-scaled as per the reference in the bottom. The range between −0.1 and 0.1 is 50

white for run P. The contour levels are 0.0, ±0.1, ±0.2, ±0.4, ±0.8, ±1.6, and ±3.2, with negative contours dashed. The green line shows Kyushu Island. The yellow line is the contour line for precipitation forecasted by run C of 10 mm h^{-1}, including areas exceeding 50 mm h^{-1}. Values on each panel are the relative nonlinearity for each variable calculated between the 16th and 26th model levels (approximately between 900 and 2200 m).

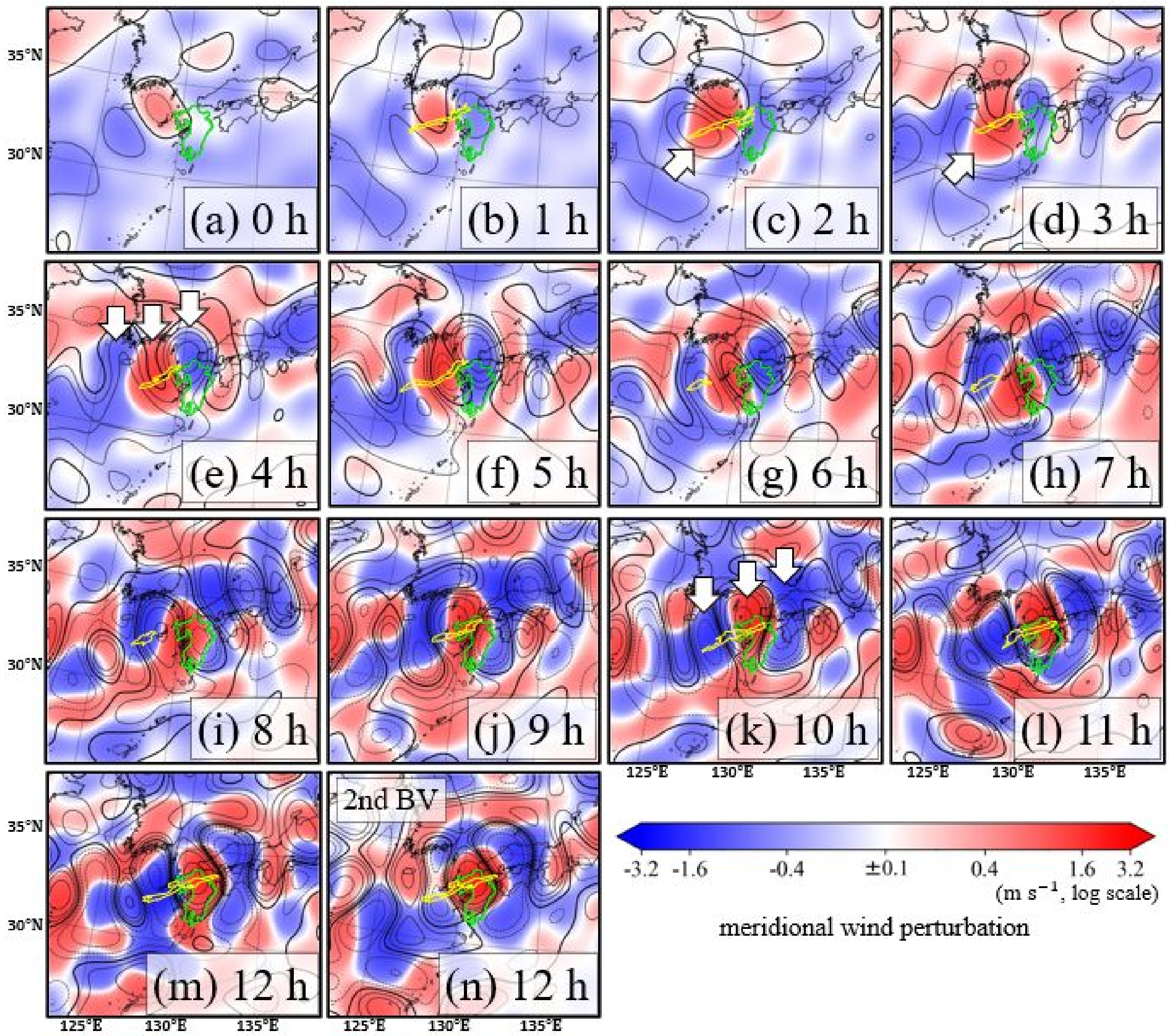

Fig. 9 Low-pass-filtered meridional wind perturbation (m s^{-1}) on the 21st model level from (a)−(m) *f* = 0 to 12 h in (color shades) run P and (contours) run N. (n) Same as (m), but based on the second bred vector. The range between −0.1 and 0.1 is white for run P. The white arrows in (c,d,e,k) are to help the explanations in the text. The yellow line is the contour line for precipitation forecasted by run C of 10 mm h^{-1}, including areas exceeding 50 mm h^{-1}.

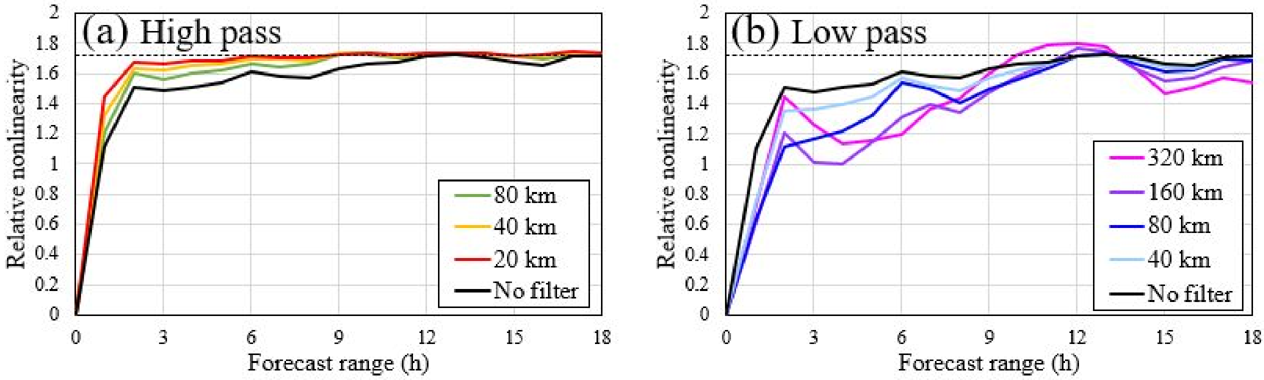

Fig. 10 Relative nonlinearity for (a) high-pass and (b) low-pass-filtered meridional wind perturbation calculated between the 16th and 26th model levels. The dotted horizontal line denotes the relative nonlinearity value of ~1.72.

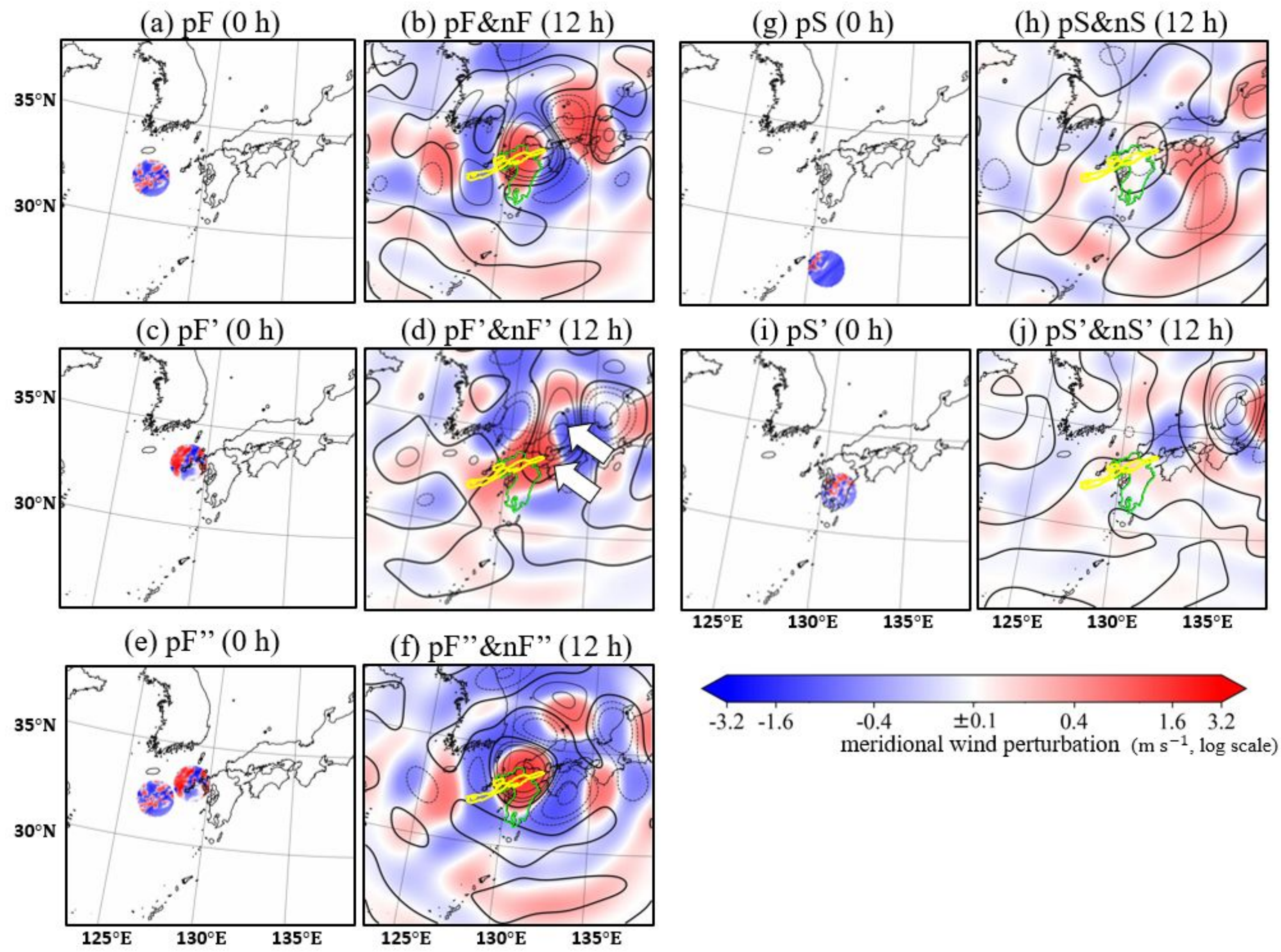

Fig. 11 (a,c,e,g,i) Meridional wind perturbation (m s^{-1}) on the 21st model level at the initial time for runs (a) pF, (c) pF', (e) pF'', (g) pS, and (i) pS'. (b,d,f,h,j) Meridional wind perturbation (m s^{-1}) on the 21st model level with low-pass spatial filtering with a cutoff wavelength of 320 km at f = 12 h for runs (b) pF and nF, (d) pF' and nF', (f) pF'' and nF'', (h) pS and nS, and (j) pS' and nS'. Solid lines indicate positive values and dotted lines indicate negative values with intervals of 0.0, ±0.1, ±0.2, ±0.4, ±0.8, ±1.6, and ±3.2 in runs nF, nF', nF'', nS, and nS'. The yellow line is the contour line for precipitation forecasted by run C of 10 mm h^{-1}, including areas exceeding 50 mm h^{-1}. The green line shows Kyushu island. The white arrows in (d) are to help the explanations in the text.

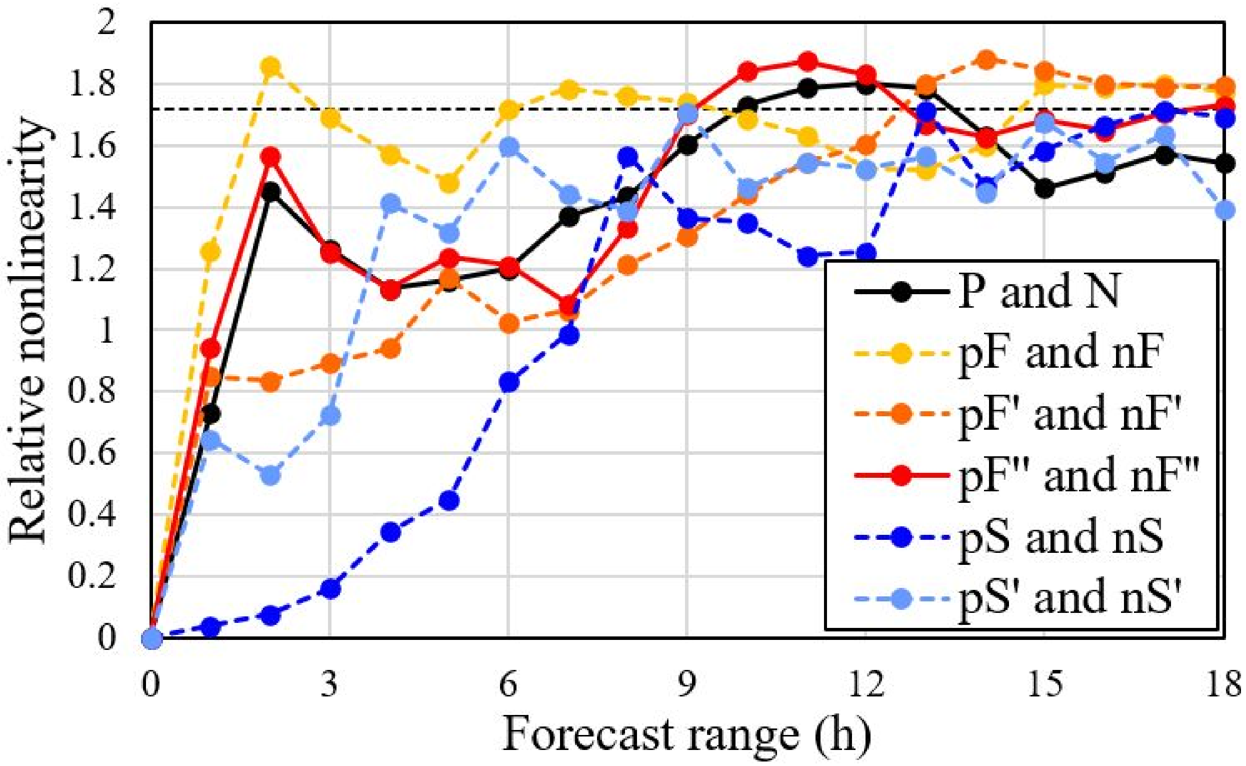

Fig. 12 Relative nonlinearity as a function of forecast time (h) for low-pass-filtered meridional wind perturbations calculated between the 16th and 26th model levels for pairs of runs (black) P and N, (yellow) pF and nF, (orange) pF' and nF', (red) pF'' and nF'', (blue) pS and nS, and (skyblue) pS' and nS'. The dotted horizontal line denotes the relative nonlinearity value of ~1.72.

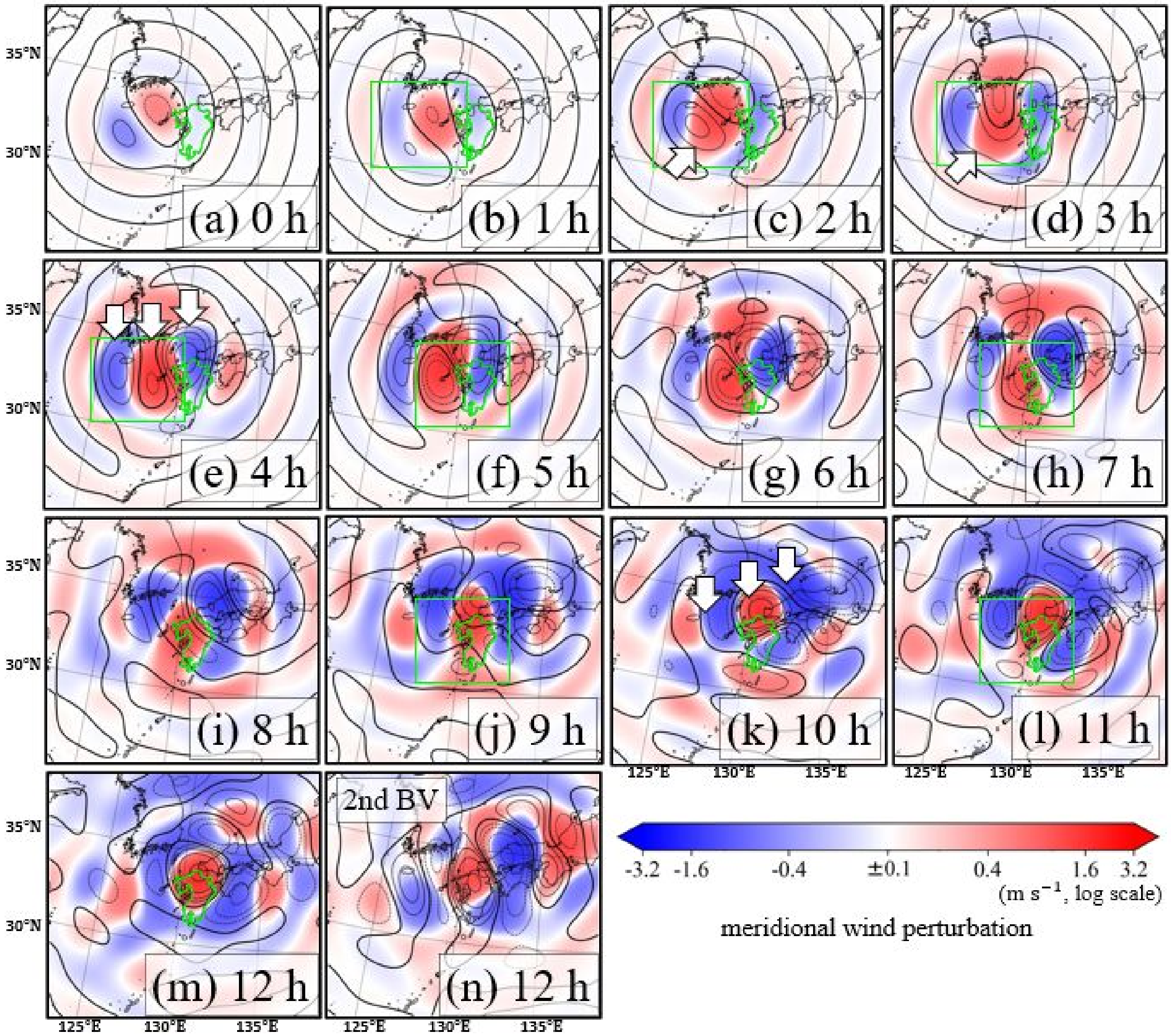

Fig. 13 Same as Fig. 9, but for runs pF'' and nF''. Green boxes show the close-up region in Figs. 14 and 15.

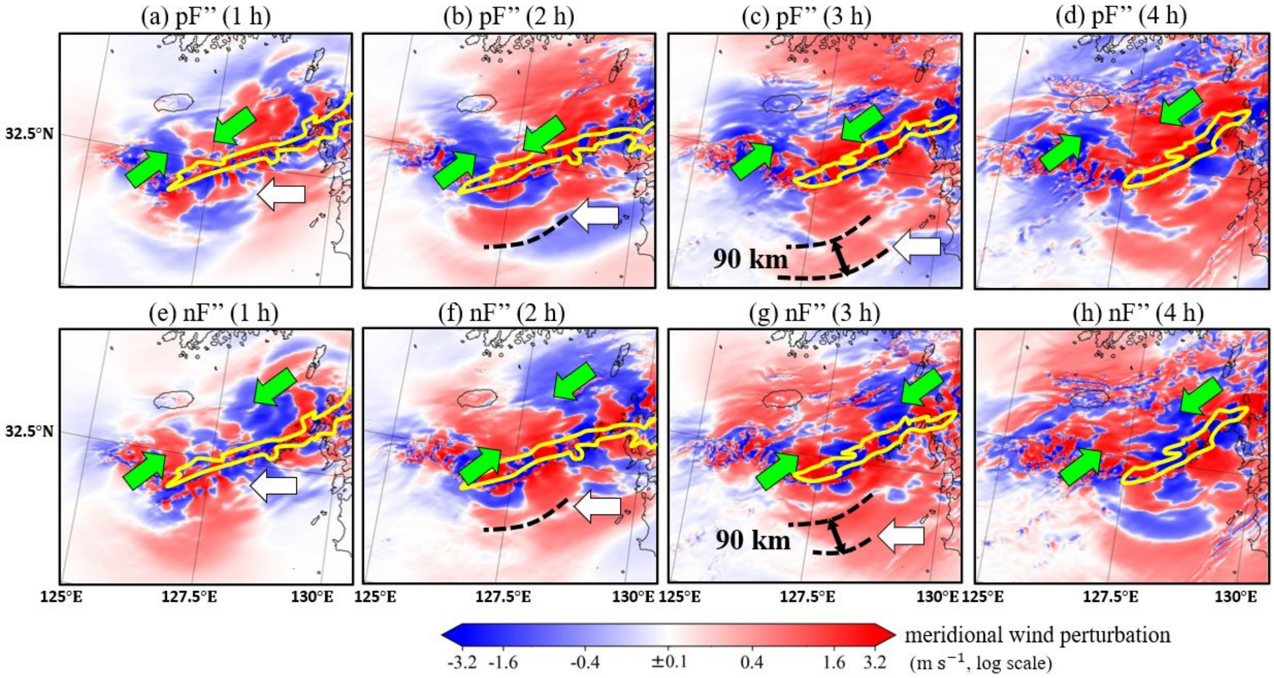

Fig. 14 Meridional wind perturbation (m s^{-1}) on the 21st model level at *f* = 1 to 4 h in run pF'' (a−d) and nF'' (e−h). The green and white arrows are to help the explanations in the text for linear and nonlinear signals, respectively. The black broken lines in (b and f) shows the tip of the positive values at *f* = 2 h. The black broken lines in (c and g) show the tips at *f* = 2 and 3 h. The yellow line shows the contour line for precipitation forecasted by run C of 10 mm h^{-1}, including areas exceeding 50 mm h^{-1}.

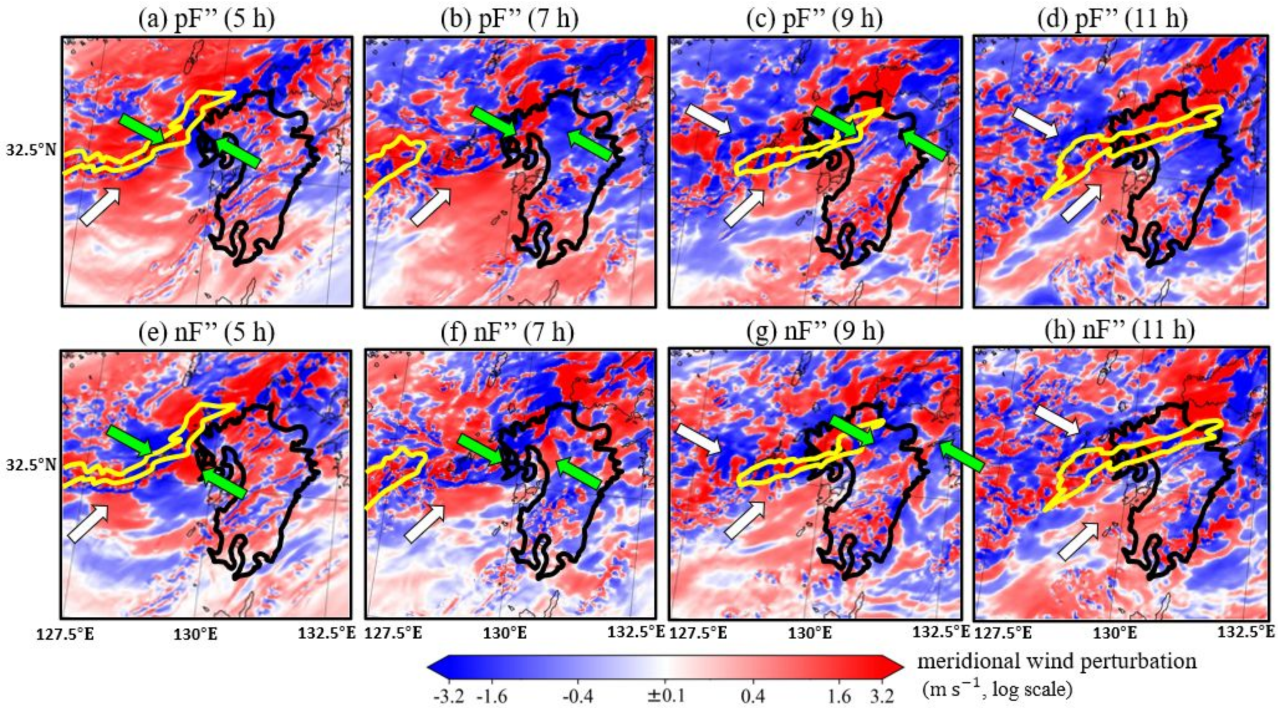

Fig. 15 Same as Fig. 14, but at *f* = 5, 7, 9, and 11 h.

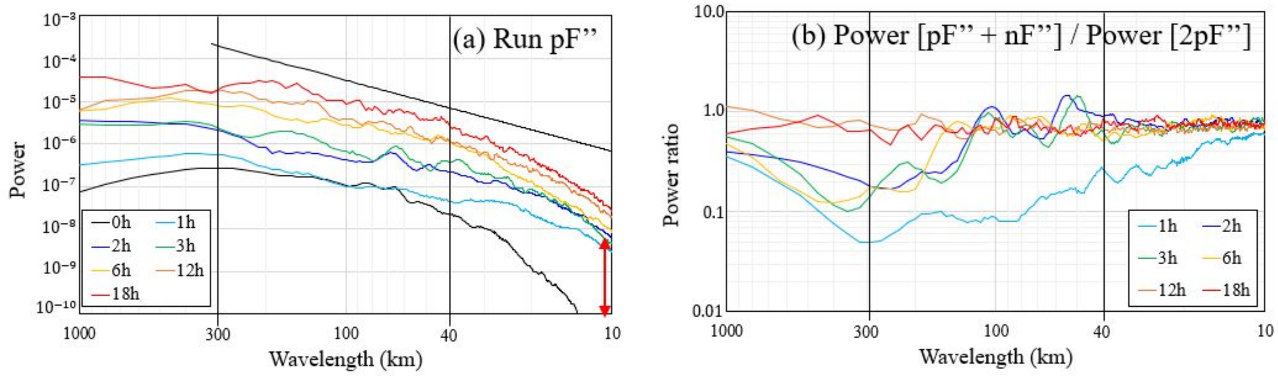

Fig. 16 Power spectra of meridional wind perturbation in (a) run pF'' and (b) ratio of between the power spectra of sum of runs pF'' and nF'' and of run pF'' with double amplitude at *f* = (black) 0, (skyblue) 1, (purple) 2, (green) 3, (yellow) 6, (orange) 12, and (red) 18 h. Black line denotes the −5/3 power law as a reference. The red arrow is to help the explanation in the text.

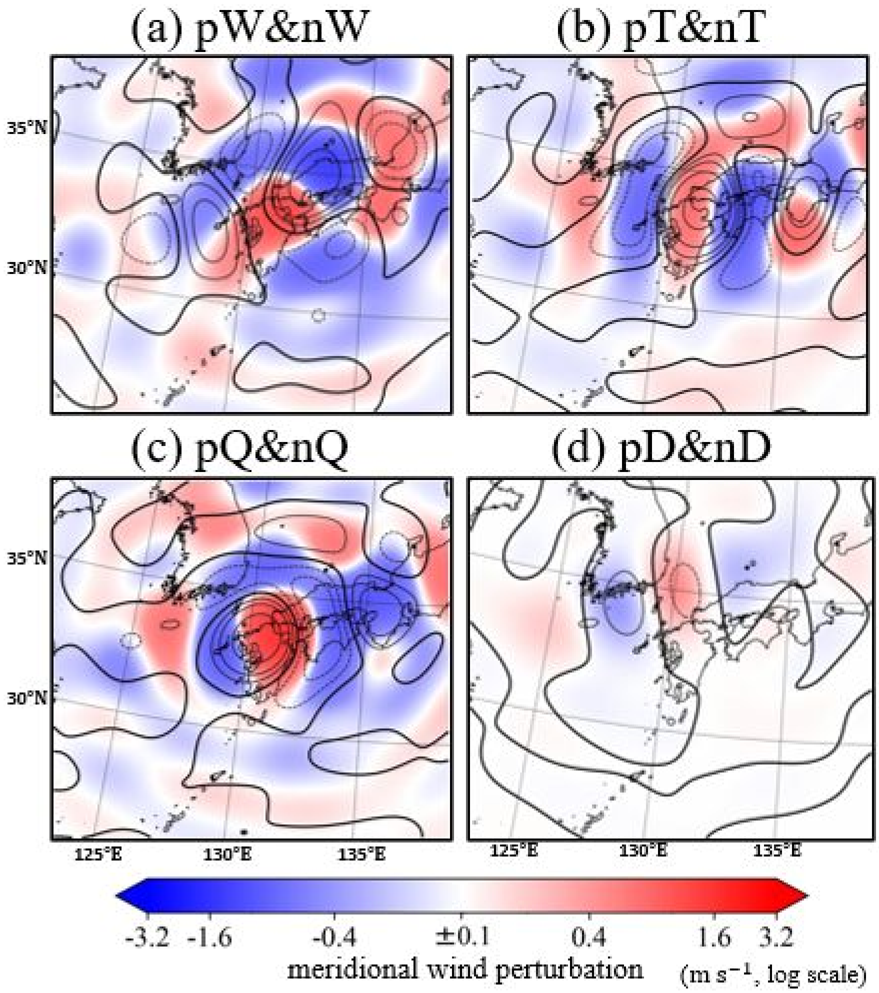

Fig. 17 Low-pass-filtered meridional wind perturbation (m s^{-1}) on the 21st model level at f = 12 h for pairs of runs (a) pW and nW, (b) pT and nT, (c) pQ and nQ, and (d) pD and nD.

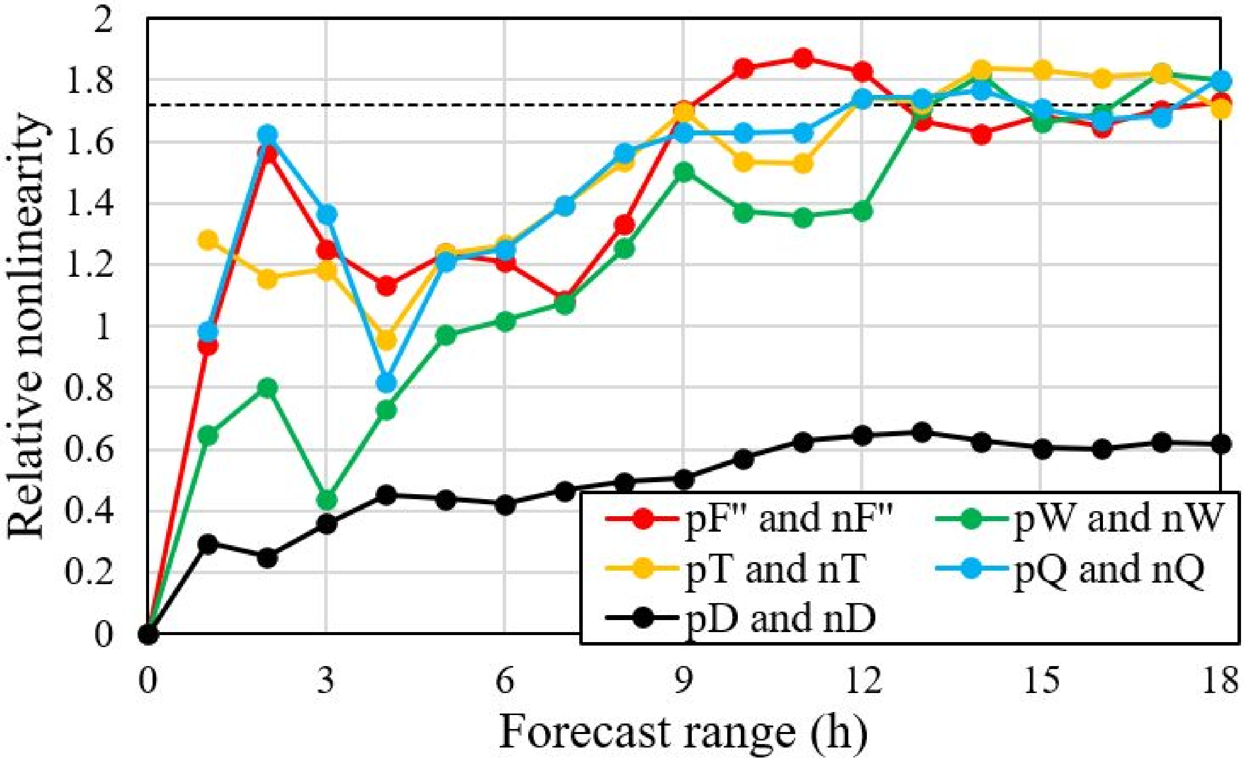

Fig. 18 Relative nonlinearity as a function of forecast time (h) for low-pass filtered meridional wind perturbations calculated between the 16th and 26th model levels for pairs of runs (red) pF'' and nF'', (green) pW and nW, (yellow) pT and nT, (skyblue) pQ and nQ, and (black) pD and nD.

List of Tables

Table 1: Experiment setting for all runs.

Run name	Perturbation	Perturbed variables	Perturbed areas	Model physics
Run C	None	N/A	N/A	All
Run N/P	First BGM	All	Entire model domain	All
Run nF/pF	First BGM	All	40-km circle around 32°N, 127°E.	All
Run nF'/pF'	First BGM	All	40-km circle around 33°N, 129°E.	All
Run nF''/pF''	First BGM	All	40-km circles around 32°N, 127°E and around 33°N, 129°E.	All
Run nS/pS	First BGM	All	40-km circle around 28°N, 131°E.	All
Run nS'/pS'	First BGM	All	40-km circle around 32°N, 131°E.	All
Run nW/pW	First BGM	Wind vector	40-km circles around 32°N, 127°E and around 33°N, 129°E.	All
Run nT/pT	First BGM	Potential temperature	40-km circles around 32°N, 127°E and around 33°N, 129°E.	All

Run nQ/pQ	First BGM	Water vapor mixing ratio	40-km circles around 32°N, 127°E and around 33°N, 129°E.	All
Run nD/pD	First BGM	All	40-km circles around 32°N, 127°E and around 33°N, 129°E.	*

BGM: breeding of growing mode.

(*) Without convective parameterization and cloud microphysics.

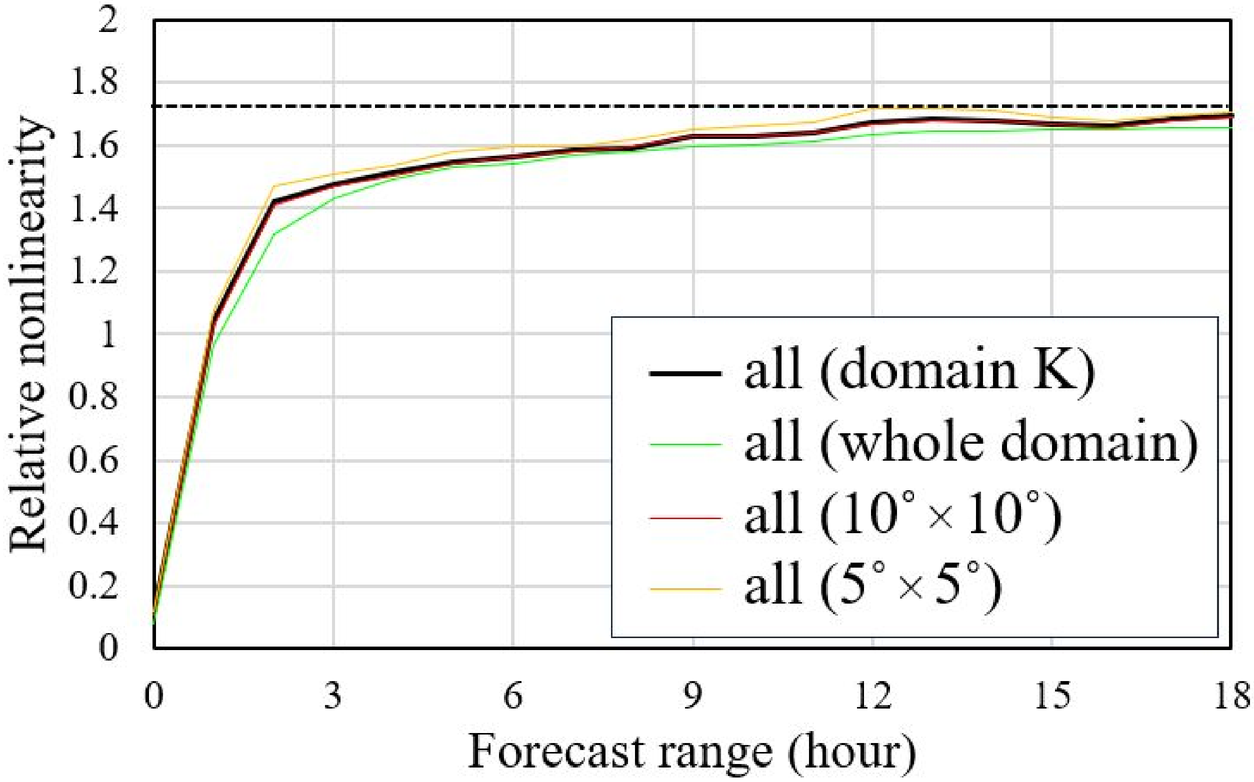

Supplement 1: Relative nonlinearity as a function of forecast time (h) between the 16th and 26th model levels. Calculated in (black) domain K (Fig. 2a), (green) the whole forecast domain, (red) the domain within 27.5°N to 37.5°N and 125°E to 135°E, and (yellow) the domain within 30°N to 35°N and 127.5°E to 132.5°E.